



HAL
open science

Global distribution and parameter dependences of gravity wave activity in the Martian upper thermosphere derived from MAVEN/NGIMS observations

Naoki Terada, François Leblanc, Hiromu Nakagawa, Alexander S. Medvedev, Erdal Yiğit, Takeshi Kuroda, Takuya Hara, Scott L. England, Hitoshi Fujiwara, Kaori Terada, et al.

► To cite this version:

Naoki Terada, François Leblanc, Hiromu Nakagawa, Alexander S. Medvedev, Erdal Yiğit, et al.. Global distribution and parameter dependences of gravity wave activity in the Martian upper thermosphere derived from MAVEN/NGIMS observations. *Journal of Geophysical Research Space Physics*, 2017, 122 (2), pp.2374-2397. 10.1002/2016JA023476 . insu-01492717

HAL Id: insu-01492717

<https://insu.hal.science/insu-01492717>

Submitted on 16 Aug 2020

HAL is a multi-disciplinary open access archive for the deposit and dissemination of scientific research documents, whether they are published or not. The documents may come from teaching and research institutions in France or abroad, or from public or private research centers.

L'archive ouverte pluridisciplinaire **HAL**, est destinée au dépôt et à la diffusion de documents scientifiques de niveau recherche, publiés ou non, émanant des établissements d'enseignement et de recherche français ou étrangers, des laboratoires publics ou privés.

RESEARCH ARTICLE

10.1002/2016JA023476

Special Section:

Major Results From the MAVEN Mission to Mars

Key Points:

- GW amplitudes in the upper thermosphere of Mars are about 2 and 10 times larger than on Venus and in low latitudes of Earth, respectively
- Amplitudes show a clear dependence on the background atmospheric temperature, suggesting saturation due to convective instability
- Dependences of the corrected amplitudes on the geographic latitude and longitude and solar wind parameters are less significant

Correspondence to:

N. Terada,
teradan@pat.gp.tohoku.ac.jp

Citation:

Terada, N., et al. (2017), Global distribution and parameter dependences of gravity wave activity in the Martian upper thermosphere derived from MAVEN/NGIMS observations, *J. Geophys. Res. Space Physics*, 122, 2374–2397, doi:10.1002/2016JA023476.

















Received 15 SEP 2016

Accepted 26 JAN 2017

Accepted article online 31 JAN 2017

Published online 15 FEB 2017

Global distribution and parameter dependences of gravity wave activity in the Martian upper thermosphere derived from MAVEN/NGIMS observations

Naoki Terada¹ , François Leblanc² , Hiromu Nakagawa¹ , Alexander S. Medvedev^{3,4} , Erdal Yiğit⁵ , Takeshi Kuroda^{1,6} , Takuya Hara⁷ , Scott L. England⁷ , Hitoshi Fujiwara⁸ , Kaori Terada¹ , Kanako Seki⁹ , Paul R. Mahaffy¹⁰ , Meredith Elrod^{10,11} , Mehdi Benna^{10,12} , Joseph Grebowsky¹⁰ , and Bruce M. Jakosky¹³ 

¹Graduate School of Science, Tohoku University, Sendai, Japan, ²LATMOS/IPSL, UPMC Univ. Paris 06 Sorbonne Universités, UVSQ, CNRS, Paris, France, ³Max Planck Institute for Solar System Research, Göttingen, Germany, ⁴Institute for Astrophysics, Georg-August-Universität, Göttingen, Germany, ⁵Department of Physics and Astronomy, George Mason University, Fairfax, Virginia, USA, ⁶Big Data Analytics Laboratory, Big Data Integration Research Center, National Institute of Information and Communications Technology, Tokyo, Japan, ⁷Space Sciences Laboratory, University of California, Berkeley, Berkeley, California, USA, ⁸Faculty of Science and Technology, Seikei University, Tokyo, Japan, ⁹Graduate School of Science, University of Tokyo, Tokyo, Japan, ¹⁰NASA Goddard Space Flight Center, Greenbelt, Maryland, USA, ¹¹CRESST, University of Maryland, College Park, College Park, Maryland, USA, ¹²CRESST, University of Maryland, Baltimore County, Catonsville, Maryland, USA, ¹³Laboratory for Atmospheric and Space Physics, University of Colorado, Boulder, Boulder, Colorado, USA

Abstract Wavelike perturbations in the Martian upper thermosphere observed by the Neutral Gas Ion Mass Spectrometer (NGIMS) onboard the Mars Atmosphere and Volatile Evolution (MAVEN) spacecraft have been analyzed. The amplitudes of small-scale perturbations with apparent wavelengths between ~100 and ~500 km in the Ar density around the exobase show a clear dependence on temperature (T_0) of the upper thermosphere. The average amplitude of the perturbations is ~10% on the dayside and ~20% on the nightside, which is about 2 and 10 times larger than those observed in the Venusian upper thermosphere and in the low-latitude region of Earth's upper thermosphere, respectively. The amplitudes are inversely proportional to T_0 , suggesting saturation due to convective instability in the Martian upper thermosphere. After removing the dependence on T_0 , dependences of the average amplitude on the geographic latitude and longitude and solar wind parameters are found to be not larger than a few percent. These results suggest that the amplitudes of small-scale perturbations are mainly determined by convective breaking/saturation in the upper thermosphere on Mars, unlike those on Venus and Earth.

1. Introduction

Internal gravity waves (GWs) are ubiquitous in the Martian atmosphere. Radio occultation measurements by Mars Global Surveyor (MGS) reported significant GW activity over the tropics and the Tharsis region in the Martian lower atmosphere at 10–30 km [Creasey et al., 2006a]. Dayglow images taken by OMEGA onboard Mars Express detected GW patterns with horizontal wavelengths of 50–150 km in the lower atmosphere [Altieri et al., 2012]. Although GW amplitudes (or fluxes) are relatively small in the lower atmosphere, GWs have appreciable effects on the large-scale winds [Medvedev et al., 2011a, 2011b, 2013, 2015], thermal balance [Medvedev and Yiğit, 2012], and density [Medvedev et al., 2016] in the mesosphere and lower thermosphere as highlighted by general circulation modeling studies, which are consistent with satellite observations. GW-induced small-scale temperature perturbations can even facilitate carbon dioxide ice cloud formations in the mesosphere and the lower thermosphere of Mars [Spiga et al., 2012; Yiğit et al., 2015a]. Aerobraking measurements by MGS and Mars Odyssey (ODY) around 100–130 km showed that GW amplitudes are highly variable with density perturbations from ~5 to 50%, and dominant wavelengths along the satellite's track of ~20–200 km [Fritts et al., 2006] or 100–300 km [Creasey et al., 2006b].

Recent measurements by the Neutral Gas and Ion Mass Spectrometer (NGIMS) [Mahaffy et al., 2014] on board the Mars Atmosphere and Volatile Evolution (MAVEN) spacecraft [Jakosky et al., 2015] have revealed that GWs prevail also in the upper thermosphere of Mars [Yiğit et al., 2015b]. Yiğit et al. [2015b] have shown using the NGIMS data obtained in December 2014 that the average amplitude of GW-induced density perturbations in the upper thermosphere is 20–40% between 180 and 220 km, and GWs are overall present up to 250 km

altitude. The authors, however, found that these maximum propagation altitudes were several tens of kilometers higher than the theoretical predictions with a whole atmosphere nonlinear spectral GW scheme [Yigit *et al.*, 2008] that considers GW dissipation due to molecular diffusion (molecular viscosity and thermal conduction) and radiative damping in addition to breaking/saturation of multiple GW harmonics due to convective instability. Similar results were obtained by linearized full-wave models with a nonbreaking wave assumption in the works of Parish *et al.* [2009], Walterscheid *et al.* [2013], and Imamura *et al.* [2016]. For instance, Imamura *et al.* [2016] estimated that a GW harmonic with a vertical wavelength of 20 km dissipates at 100–150 km, while that with a very long vertical wavelength of ~ 100 km can penetrate up to ~ 250 km.

Gravity waves are excited in the troposphere by a variety of mechanisms. They include flow over topography, instabilities of jets and weather systems, and atmospheric convection. These sources generate the gravity wave field in the lower atmosphere with complex spatiotemporal and spectral characteristics, which were recently explored with a high-resolution Martian general circulation model (GCM) [Kuroda *et al.*, 2016]. In addition to the propagation of GWs from below, which falls into the broad range of internal wave coupling processes [Yigit and Medvedev, 2015], solar wind forcing from above is another important physical mechanism that can cause thermospheric disturbances [Yigit *et al.*, 2016]. In the terrestrial thermosphere, Traveling Atmospheric Disturbances (TADs) are generated by magnetospheric energy deposition [Prölss, 1993; Hocke and Schlegel, 1996] or by lower atmospheric forcing [Vadas and Liu, 2009, and references therein]. The magnetospheric energy is deposited mainly in the form of Joule heating and particle precipitations [Knipp *et al.*, 2004]. It generates disturbances in the polar lower thermosphere, propagating away from the source region with a slightly upward angle to the horizontal. They, thus, transport energy and momentum from the polar regions to the middle and low latitudes and from the lower thermosphere to the upper thermosphere [Gardner and Schunk, 2010]. Large-scale TADs (horizontal scales greater than ~ 1000 km) propagate long distances (more than several thousands of kilometers), although those having a relatively short wavelength are preferentially dissipated and restricted near the source region [Mayr *et al.*, 1990]. Most of large-scale TADs can be generated by the energy deposition from the magnetosphere [Prölss, 1993; Hocke and Schlegel, 1996], but some of them are observed independently of geomagnetic activity [Tsugawa *et al.*, 2004; Vadas and Liu, 2009]. Numerical modeling and satellite- and ground-based observations have intensively been used for investigating the solar wind and lower atmospheric forcing of terrestrial thermospheric disturbances [e.g., Fujiwara and Miyoshi, 2006, 2009; Miyoshi *et al.*, 2014], but the relative importance of the GW sources is still insufficiently understood, mainly because of an insufficient number of global observations in the thermosphere. In the case of Mars, solar wind forcing is expected to appear in a different way due to the lack of a planetary-scale magnetic field. A direct interaction of the solar wind with the Martian upper atmosphere induces a significant energy deposition in the form of precipitation of pickup ions [Luhmann and Kozyra, 1991; Leblanc and Johnson, 2002; Chaufray *et al.*, 2007; Fang *et al.*, 2013]. Contrary to Earth, where magnetospheric energy deposition is concentrated in the polar regions, pickup ion precipitation on Mars occurs in a wide area of the thermosphere. A modeling study by Fang *et al.* [2013] predicted that precipitating pickup O^+ ions generate appreciable disturbances in a wide area of the Martian upper thermosphere, which are yet to be observationally confirmed.

Thermal effects of GWs play a major role in determining temperature profiles in the Martian mesosphere and lower thermosphere [Medvedev and Yigit, 2012; Medvedev *et al.*, 2015] and in the upper thermosphere [England *et al.*, 2016], which is of great importance for understanding the reservoir region for atmospheric escape [S. Bougher *et al.*, 2015]. Overall, GWs can produce net thermal effects in the upper atmosphere, which manifest as heating in the mesosphere and lower thermosphere and cooling at higher altitudes, exceeding 150 K d^{-1} in the terrestrial thermosphere [Yigit and Medvedev, 2009] and 150 K sol^{-1} in the Martian thermosphere [Medvedev and Yigit, 2012; Medvedev *et al.*, 2015] in a zonally and temporally averaged sense. The significance of both dynamical and thermal GW effects was shown in the work of Medvedev and Yigit [2012] who have demonstrated that accounting for them in the GCM had allowed for reproducing the latitudinal temperature distribution obtained from the ODY aerobraking measurements. However, there are still large uncertainties in the detailed thermal budget of the Martian thermosphere, including the radiative cooling in the CO_2 $15 \mu\text{m}$ bands, the main cooling mechanism in the lower thermosphere [cf. S. W. Bougher *et al.*, 2015; Terada *et al.*, 2016]. Forbes *et al.* [2006] pointed out that the thermospheric temperature response to the 27 day variation in the solar EUV flux on Mars is 4 to 7 times larger than that on Venus, suggesting that the CO_2 $15 \mu\text{m}$ radiative cooling is less effective in the Martian thermosphere. The authors noted that such a

comparison among the terrestrial planets gives an important clue for constraining the heating/cooling mechanisms in the upper atmospheres of these planets.

The purposes of this paper are to investigate the global distribution and parameter dependences of the small-scale wave activity in the Martian upper thermosphere using MAVEN/NGIMS data and to compare the wave amplitudes in the upper thermospheres of Mars, Venus, and Earth in order to provide observational constraints on the wave dissipation processes, heating/cooling processes, and sources of upper thermospheric perturbations. The organization of this paper is as follows: Section 2 describes the data and analysis method used in this study. Section 3 presents results of the analysis of small-scale perturbations in various coordinate systems. In Section 4, physical basis of the wave amplitude dependence on the background temperature is discussed, and the global distribution and parameter dependences of the “corrected amplitude” are given. Section 5 summarizes our major results and conclusions.

2. Data and Analysis Method

Neutral gas density profiles obtained from in situ measurements by MAVEN/NGIMS in the Martian upper thermosphere from 11 February 2015 to 31 March 2016 are analyzed. NGIMS data obtained between October and December in 2014 are also available but not used in the present statistical analysis, because different operating settings were used during this period. In the beginning of the mission (October 2014 to December 2014), NGIMS was initially set with the multipliers at the higher voltage setting of 125 V in order to be able to collect as much neutral signal as possible. Our goal at the time was to get possible signal from lower signal species like HDO and Kr. However, in early December of 2014, NGIMS began to experience contamination on m19 and m16 channel causing a loss of signal across all masses. We quickly corrected the problem making a series of changes to our settings including lowering the multiplier voltage to 25 V. While this does indicate a slightly lower overall signal to all masses, it is also a cleaner signal. As a result NGIMS data from 2014 have different calibration techniques and methods of computation than those from February 2015 and forward. The nominal periapsis altitude, apoapsis altitude, orbital period, and inclination of MAVEN are approximately 150 km, 6220 km, 4.5 h, and 75°, respectively [Jakosky *et al.*, 2015]. The periapsis occasionally goes down to ~130 km during “deep dip” campaigns. Below 500 km, NGIMS measures neutrals and ions using the closed and open sources [Mahaffy *et al.*, 2014, 2015; Benna *et al.*, 2015]. In this study, ^{40}Ar density profiles obtained with the closed source (Level 2 data, version 6, revision 2) are used to examine small-scale perturbations in the upper thermosphere, since Ar measurements are less affected by background gases in the instrument. Changes in NGIMS data from version 3 (all revisions) [e.g., Yiğit *et al.*, 2015b] to version 6, revision 2, were significant. In version 3, revision 2, the data were not yet interpolated to a constant cadence of 1 s. This was done for better comparison between all the neutral species and to improve saturation correction. From versions 4 to 6, the NGIMS team went through a series of calibrations and modeling efforts that determined new fractionation patterns and background subtraction methods that significantly effected the determination of neutral densities of all species particularly Ar, CO_2 , CO, N_2 , and oxygen-related species. These revisions were based on calibration gas experiments done in flight, data collected throughout the mission and comparison with other neutral instrument data gathered by MAVEN (Imaging Ultraviolet Spectrograph (IUVS) and Accelerometer (ACC)). Note that Ar behaves similarly to CO_2 , the main constituent of the Martian atmosphere: Their masses are close, Ar number density is about 60 times smaller, and amplitudes and phases of density perturbations are similar (cf. Figure 2 of S. Bougher *et al.* [2015]; England *et al.* [2016]). Number density of Ar at the periapsis varies from $N(\text{Ar}) \sim 10^7$ to $\sim 10^9 \text{ cm}^{-3}$, since the periapsis altitude goes down during deep dips and changes with season and location due to the precession of the satellite orbit. To give a physical basis to the number density range analyzed here, we restrict ourselves to examining the region around the exobase: Only the number density range between $N(\text{Ar}) = 10^5$ and 10^7 cm^{-3} is analyzed. The lower altitude limit, where $N(\text{Ar}) = 10^7 \text{ cm}^{-3}$, corresponds to 160–180 km altitudes on the dayside and 150–160 km altitudes on the nightside, while the upper altitude limit, where $N(\text{Ar}) = 10^5 \text{ cm}^{-3}$, corresponds to 200–290 km altitudes on the dayside and 160–240 km altitudes on the nightside. These altitude ranges straddle the exobase altitudes. Note that $N(\text{Ar}) \sim 10^5\text{--}10^6 \text{ cm}^{-3}$ corresponds to the exobase for Ar and CO_2 and $N(\text{Ar}) \sim 10^7 \text{ cm}^{-3}$ to the exobase for hot O. The exobase altitudes vary depending on species. For instance, dayside averaged exobase altitudes calculated for a solar minimum condition in the work of Terada *et al.* [2016] are 172, 190, 202, 194, and 182 km for hot O, thermal O, CO_2 , N_2 , and H,

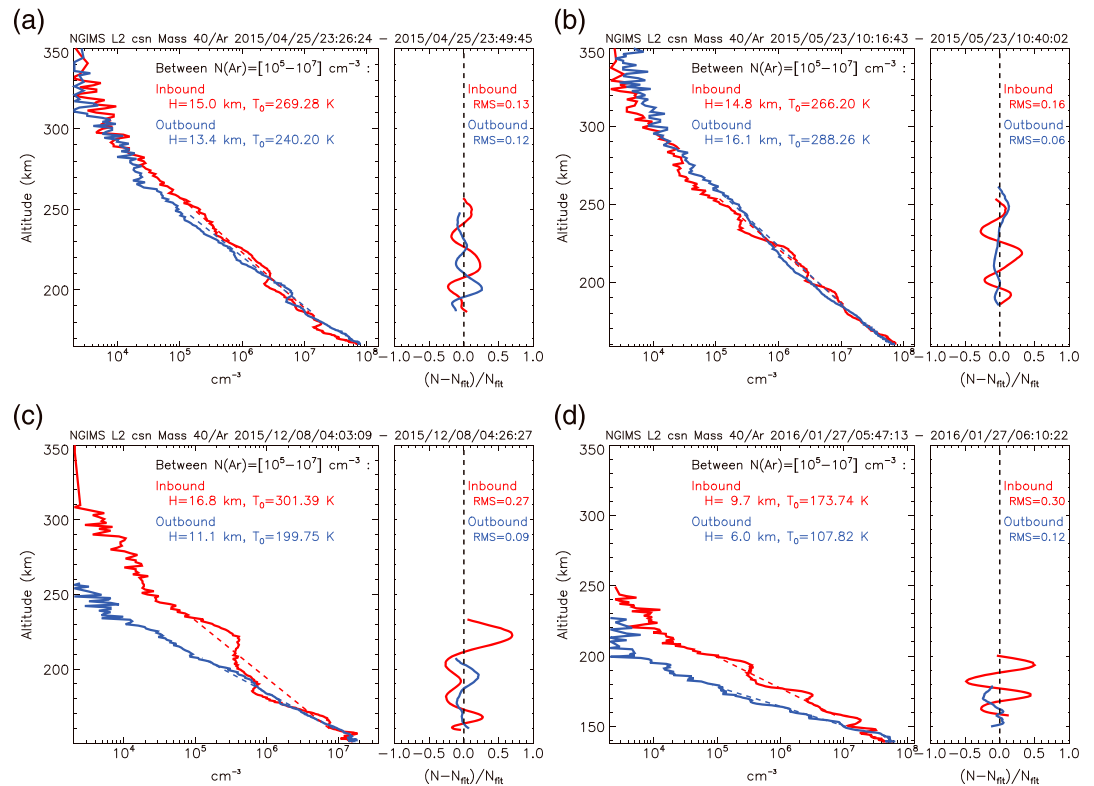


Figure 1. Examples of NGIMS Ar density observation in the Martian upper thermosphere along (a) Orbit #1106 on 25 April 2015 at $L_s = 332^\circ$, (b) Orbit #1254 on 23 May 2015 at $L_s = 347^\circ$, (c) Orbit #2314 on 8 December 2015 at $L_s = 79^\circ$, and (d) Orbit #2580 on 27 January 2016 at $L_s = 101^\circ$. Left panel of each two-panel plot illustrates Ar number density profiles during inbound (red curve) and outbound (blue curve) legs. A red (blue) dashed line shows a fit to the inbound (outbound) density profile assuming a constant scale height. Right panel of each two-panel plot shows the residual-to-fit ratio, $(N - N_{fit})/N_{fit}$. Scale height (H) and temperature (T_0) of thermospheric Ar are indicated in the left panels and RMS amplitudes of the perturbations in the right panels. The locations of MAVEN at which NGIMS measured Ar number density of 10^5 cm^{-3} were (a) at $\text{SAZ} = 24^\circ$, $\text{MSO longitude} = -21^\circ$, $\text{latitude} = -12^\circ$ for inbound leg and at $\text{SAZ} = 25^\circ$, $\text{MSO longitude} = 6^\circ$, $\text{latitude} = 24^\circ$ for outbound leg; (b) at $\text{SAZ} = 66^\circ$, $\text{MSO longitude} = -63^\circ$, $\text{latitude} = -25^\circ$ for inbound leg and at $\text{SAZ} = 40^\circ$, $\text{MSO longitude} = -38^\circ$, $\text{latitude} = 15^\circ$ for outbound leg; (c) at $\text{SAZ} = 76^\circ$, $\text{MSO longitude} = -75^\circ$, $\text{latitude} = 22^\circ$ for inbound leg and at $\text{SAZ} = 83^\circ$, $\text{MSO longitude} = -82^\circ$, $\text{latitude} = -17^\circ$ for outbound leg; and (d) at $\text{SAZ} = 99^\circ$, $\text{MSO longitude} = -118^\circ$, $\text{latitude} = 70^\circ$ for inbound leg and at $\text{SAZ} = 120^\circ$, $\text{MSO longitude} = -129^\circ$, $\text{latitude} = 36^\circ$ for outbound leg.

respectively, and the altitude difference between species increases with solar activity. For the solar activity during the period analyzed here (moderate solar activity), dayside averaged exobase altitudes are estimated to be $\sim 220 \text{ km}$ for Ar and CO_2 and $\sim 180 \text{ km}$ for hot O based on the model of *Terada et al.* [2016].

In this study, a method similar to the one used for analyzing wavelike perturbations in the Venusian upper thermosphere [Kasprzak et al., 1988] is applied. This enables us to evenly compare the upper thermospheric perturbations between Mars and Venus. The analysis method consists of four steps: Step 1 is to remove altitude trends assuming a constant scale height (for inbound and outbound legs separately). Step 2 is to apply a long-period smoothing with a 110 s (corresponding to $\sim 500 \text{ km}$ along MAVEN's track) moving average filter to the detrended profile obtained in Step 1. Step 3 is to obtain the difference of Step 1 minus Step 2. Finally, Step 4 is to apply a short-period smoothing with a 26 s (corresponding to $\sim 100 \text{ km}$ along the track) moving average filter. These steps allow for analyzing perturbations having "apparent wavelengths" between ~ 100 and $\sim 500 \text{ km}$. Here the apparent wavelength means the wavelength measured along MAVEN's track. If we assume that the observed structures are due to vertical rather than horizontal variations, these apparent wavelengths correspond to the waves having vertical wavelengths between ~ 10 and $\sim 50 \text{ km}$, because the slope (vertical to horizontal ratio) of MAVEN's track is $\sim 1/10$ in the altitude range considered here. If horizontal variations are assumed, they correspond to the waves having horizontal wavelengths between ~ 100 and $\sim 500 \text{ km}$. Since these wavelengths are rather short, atmospheric perturbations analyzed in this study are

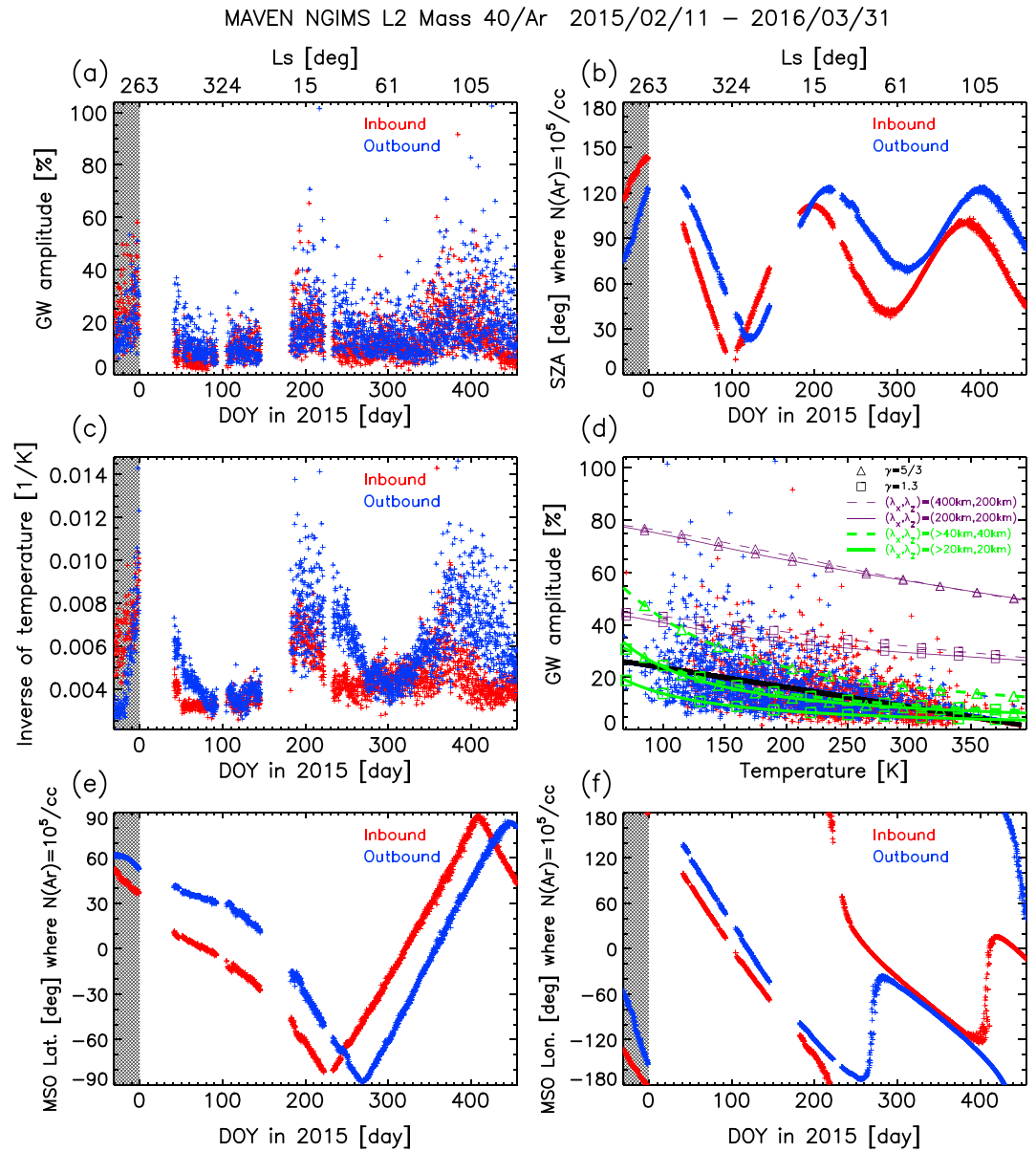


Figure 2. (a) GW amplitudes obtained from Ar density profiles between 11 February 2015 and 31 March 2016. The red and blue plus symbols mark those obtained in inbound and outbound legs, respectively. (b) The SZA of MAVEN's position at which NGIMS measured $N(\text{Ar}) = 10^5 \text{ cm}^{-3}$. (c) The inverse of the upper thermospheric temperature (T_0^{-1}). (d) Correlation between the GW amplitudes and T_0 . The linear regression lines for inbound (red line), outbound (blue line), and all legs (black line) are plotted, although these three lines are almost completely overlapped. Also plotted are the theoretical thresholds for the breaking/saturation of GWs due to convective instability for $(\lambda_x, \lambda_z) = (>20 \text{ km}, 20 \text{ km})$, $(>40 \text{ km}, 40 \text{ km})$, $(200 \text{ km}, 200 \text{ km})$, and $(400 \text{ km}, 200 \text{ km})$ obtained from equation (2), with green solid, green dashed, violet solid, and violet dashed curves, respectively. Those obtained assuming $\gamma = 5/3$ are indicated with triangles, and $\gamma = 1.3$ with squares. (e) The MSO latitude and (f) longitude of MAVEN's position at which NGIMS measured $N(\text{Ar}) = 10^5 \text{ cm}^{-3}$. The cross-hatched areas in Figures 2a, 2b, 2c, 2e, and 2f indicate the values measured in December 2014, which are not used in the statistical analysis. Areocentric longitude (L_s) is indicated on the top of Figures 2a and 2b.

primarily interpreted as gravity waves (GWs). The possibility of acoustic wave modes was discussed in the work of England *et al.* [2016], who used a linear two-fluid model and found it to be less probable. Figure 1 displays examples of the Ar density observations by NGIMS. The left panels illustrate Ar density profiles for inbound (red curve) and outbound (blue curve) legs. Error bars are indicated with horizontal lines, although they are too short to see. The red (blue) dashed line shows the least squares linear fit to the inbound (outbound) density profile performed in Step 1. This fitting is performed using a density profile

segment that satisfies $N(\text{Ar}) > 10^4 \text{ cm}^{-3}$. The obtained scale height (H) and temperature (T_0) of Ar in the upper thermosphere are indicated in the left panels. H and T_0 generally decrease with increasing solar zenith angle (SZA) but are sometimes elevated due to short-term, seasonal, localized variations, etc. The right panels show the residual-to-fit ratios, $(N - N_{\text{fit}})/N_{\text{fit}}$, obtained after applying Steps 1 to 4. Perturbations having vertical wavelengths of $\sim 20\text{--}40$ km (if we assume that the observed structures are due to vertical variations) are easily recognized. The root-mean-square (RMS) amplitudes of $(N - N_{\text{fit}})/N_{\text{fit}}$ are 6–30% in these examples. Wavelike perturbations are commonly observed, while pulse-like disturbances, like a large-amplitude perturbation around 225 km in the inbound leg of Figure 1c, are also observed in some orbits. These features are quite similar to the perturbations observed in the Venusian thermosphere [Kasprzak *et al.*, 1988].

3. Results

Figure 2 illustrates GW amplitudes (RMS amplitudes of $(N - N_{\text{fit}})/N_{\text{fit}}$) obtained from the four steps explained in the previous section. The numbers of data points are 1659 for both inbound and outbound legs (3318 in total) between February 2015 and March 2016. GW amplitudes represent short- to long-term variability. About 20% of short-term variations (less than a few days) are superimposed on a middle- to long-term trend (tens to a few hundreds of days) for both inbound and outbound legs, as one can see in Figure 2a. The amplitudes range from ~ 0 to $\sim 100\%$, and their average is 15.1% between February 2015 and March 2016. The cross-hatched area in Figure 2 indicates GW amplitudes obtained in December 2014, which are not used in the present statistical analysis but shown to compare with the result of Yiğit *et al.* [2015b]. Yiğit *et al.* [2015b] analyzed the NGIMS data obtained in December 2014 and showed that average GW amplitudes were 20–40% during that period. Although Yiğit *et al.* [2015b] employed a different method (a seventh-order polynomial fitting) to derive the GW amplitudes, their values are similar to those obtained in our study in the same period. If we employ a seventh-order polynomial fit [Yiğit *et al.*, 2015b] instead of linear fits with a constant scale height in Step 1, and then Steps 2 to 4 are applied, we obtain the average amplitude of 14.2% between February 2015 and March 2016. If we use a seventh-order polynomial fit in Step 1, and Steps 2 to 4 (wavelength filters) are not applied, the average amplitude of 20.4% is obtained. Figure 2b shows the SZA of MAVEN's position at which NGIMS measured Ar number density of 10^5 cm^{-3} . The SZA varies from 10° to 124° with a ~ 200 day periodicity as MAVEN's periapsis precesses around the planet (see Figure 17 of Jakosky *et al.* [2015] for the track of MAVEN's periapsis location). The inverses of the upper thermospheric temperatures (T_0^{-1}), which are obtained from Step 1 in the previous section, are plotted in Figure 2c. T_0^{-1} positively correlates with the SZA, since the upper thermospheric temperature T_0 generally decreases with increasing SZA. T_0 is about 200–350 K on the dayside and 100–200 K on the nightside. T_0^{-1} also positively correlates with the GW amplitudes. Figure 2d illustrates correlation between the GW amplitudes and T_0 , showing that they are moderately correlated (correlation coefficient is -0.47). Note that this correlation coefficient is somewhat reduced by the large-amplitude short-term variations. If we use daily-averaged values of the GW amplitudes and T_0 , we obtain a correlation coefficient of -0.7 between them. Linear regression lines for the inbound (red line), outbound (blue line), and all legs (black line) are illustrated in Figure 2d. These three lines are almost completely overlapped (the red and blue lines are behind the black line), suggesting that the T_0 dependence is a persistent feature. The green and violet curves in Figure 2d indicate theoretical thresholds for the breaking/saturation of GWs due to convective instability [Lindzen, 1973; Fritts, 1984; Smith *et al.*, 1987; Fritts and Alexander, 2003], which will be discussed in section 4.1. Note that instabilities of GW harmonics can occur at any amplitude, and the theoretical threshold represents only a suitable estimate [Sonmor and Klaassen, 1997].

The upper thermospheric temperature T_0 is known to vary not only with SZA but also shows dawn-dusk asymmetry, often with a warmer temperature in the afternoon sector [e.g., González-Galindo *et al.*, 2009; S. W. Bougher *et al.*, 2015]. For instance, MAVEN was located in the afternoon sector near the periapsis and observed relatively high T_0 around the day of year of 40 to 90 in 2015, compared to the temperatures at similar SZA observed in the later period (see Figures 2b and 2c). Many of the discrepancies between the long-term trends in the SZA variations (Figure 2b) and the T_0^{-1} variations (Figure 2c) are attributable to the dawn-dusk asymmetry in T_0 and its seasonal variation, which were reproduced in thermospheric GCMs [e.g., González-Galindo *et al.*, 2009; S. W. Bougher *et al.*, 2015]. However, T_0 also shows temporal variations responding to short- (less than a few days) to middle-term (less than a month) variations in Sun's EUV flux. Figure 3

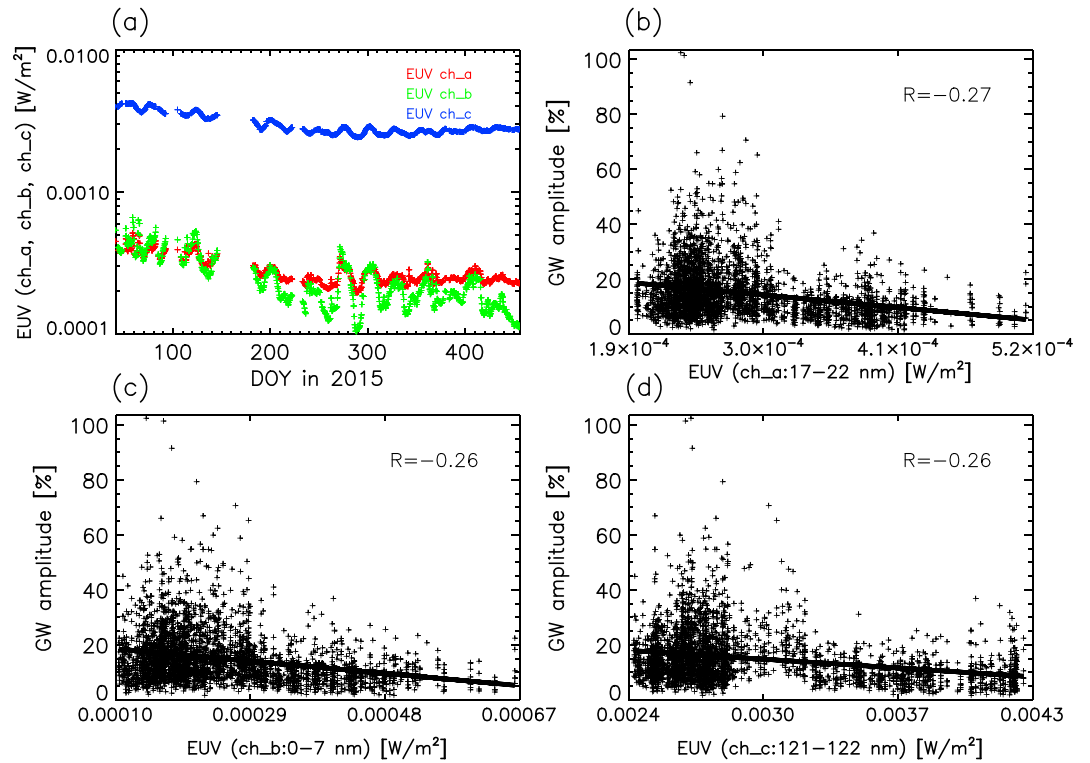


Figure 3. (a) Sun’s EUV irradiances measured by the MAVEN/EUV monitor in Channel A (17–22 nm), Channel B (0.1–7 nm), and Channel C (121–122 nm) from 11 February 2015 to 31 March 2016. (b–d) The GW amplitudes plotted as a function of EUV irradiance for each channel. The black plus symbols mark the GW amplitudes, and the black line shows the linear regression line. The correlation coefficient (R) is indicated in each diagram.

illustrates the variations in Sun’s EUV irradiances measured by the MAVEN/EUV monitor [Eparvier et al., 2015] and their correlations with the GW amplitudes. The data distributions in Figure 3 (especially Figure 3d) are not uniform, and weak or almost no anticorrelations with the correlation coefficients of -0.26 to -0.27 are observed. GW amplitudes tend to decrease with increasing EUV irradiances, suggesting that higher EUV irradiances produce higher thermospheric temperatures, and thus reduced GW amplitudes. They also decrease due to the enhanced dissipation by molecular diffusion, whose coefficient increases with the EUV flux and the thermospheric temperature T_0 [Yigit and Medvedev, 2010]. The correlation coefficients between the GW amplitudes and T_0 , SZA, EUV irradiances, and solar wind parameters are summarized in Table 1. The correlations with T_0 and SZA are found to be stronger than the others.

Table 1. Correlation Coefficients Between the GW Amplitudes and Upper Thermospheric Temperature (T_0), SZA Where NGIMS Measured $N(Ar) = 10^5 \text{ cm}^{-3}$, Solar EUV Irradiances Measured in Channel A (17–22 nm), Channel B (0.1–7 nm), and Channel C (121–122 nm), Solar Wind Dynamic Pressure, Solar Wind Density, and Solar Wind Velocity for the Inbound, Outbound, and All Legs^a

	Inbound	Outbound	All
T_0	-0.47	-0.42	-0.47
T_0 (daily averaged)	-0.67	-0.67	-0.70
SZA where $N(Ar) = 10^5 \text{ cm}^{-3}$	0.48	0.40	0.47
EUV Channel A (17–22 nm)	-0.28	-0.27	-0.27
EUV Channel B (0.1–7 nm)	-0.26	-0.27	-0.26
EUV Channel C (121–122 nm)	-0.31	-0.23	-0.26
Solar wind dynamic pressure	-0.08	-0.08	-0.07
Solar wind density	-0.09	-0.10	-0.09
Solar wind velocity	0.00	-0.03	-0.01

^aCorrelation coefficient between the daily-averaged GW amplitudes and T_0 is also shown.

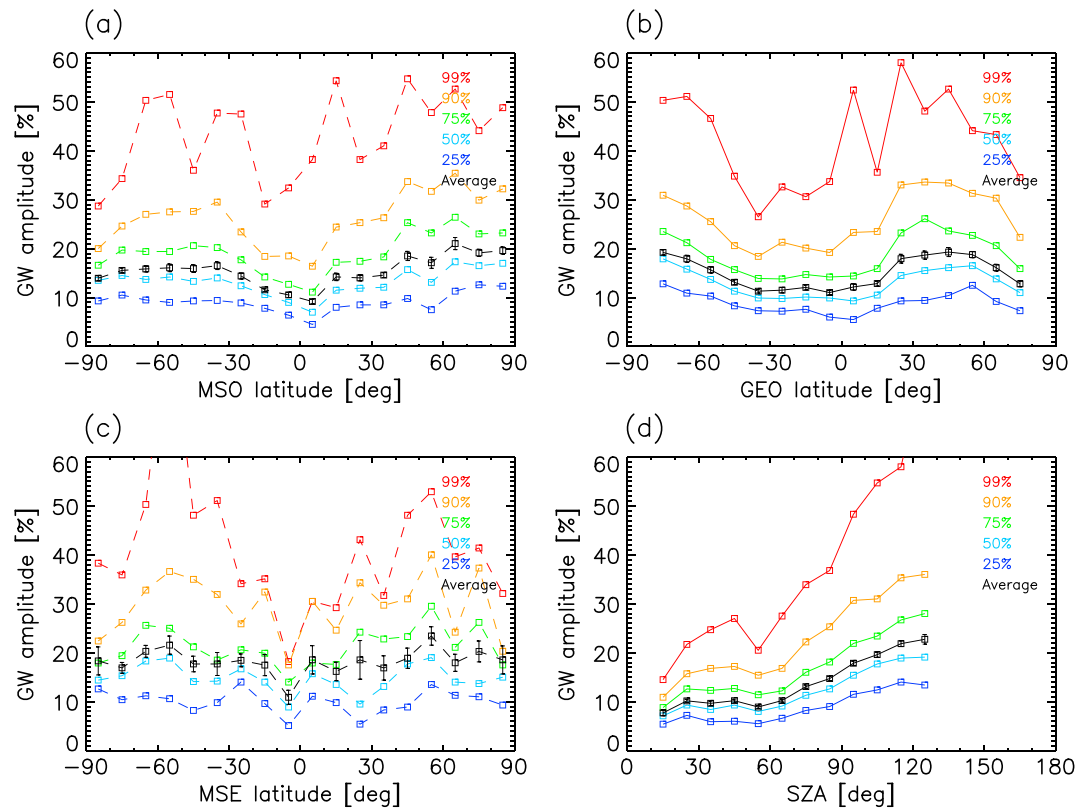


Figure 4. (a) The average (black curve), 99th percentile (red curve), 90th percentile (orange curve), 75th percentile (green curve), 50th percentile (light blue curve), and 25th percentile (dark blue curve) of the GW amplitudes as functions of latitude in the MSO coordinate. The standard error is shown by vertical bars on the curve representing the average amplitude. (b–d) Same as Figure 4a except in the GEO coordinate, in the MSE coordinate, and as functions of SZA, respectively. The GW amplitudes in the MSO coordinate (Figures 4a) and MSE coordinate (Figure 4c) are illustrated with dashed curves, because the data coverage is insufficient and localized in these coordinates (see Figures 6a and 6c).

Figure 4 displays the average (black curve) and percentiles (colored curves) of the GW amplitudes as functions of latitudes in the Mars-centered Solar Orbital (MSO) coordinate system, where the x axis points from Mars toward the Sun, the z axis is perpendicular to the Martian orbital plane, and the y axis points opposite to the Martian orbital velocity vector, completing the right-handed coordinate system, the Geographic (GEO) coordinate system, and the Mars-centered Solar Electric field (MSE) coordinate system, where the motional electric field embedded in the solar wind is parallel to the z axis, the x axis points from Mars toward the Sun, and the y axis completes the right-handed coordinate system, and as functions of SZA. The positions of 0° longitudes (east positive) and 0° latitudes (north positive) in the MSO and MSE coordinates are located at the subsolar point in this study. Conversion to the MSE coordinate is performed only when the change in the clock angle of interplanetary magnetic field (IMF) measured in the solar wind region was less than 30° between inbound and outbound legs. Because the IMF data are unavailable when the apoapsis of MAVEN is inside the induced-magnetosphere or magnetosheath, the number of the data points in the MSE coordinate is smaller (~600 data points) than those in the MSO and GEO coordinates (~3300 data points). The GW amplitudes in the MSO coordinate (Figures 4a) and MSE coordinate (Figure 4c) are illustrated with dashed curves, because the data coverage is insufficient and localized in these coordinates (see Figures 6a and 6c). We see a clear SZA dependence in Figure 4d, which is more prominent than the latitudinal dependences in Figures 4a–4c. The average amplitude varies from ~10% on the dayside (SZA < 50°) to ~20% on the nightside (SZA = 100°–120°). It is interesting to note that *Creasey et al.* [2006b] found larger density fluctuations during the day in the lower thermosphere using the MGS accelerometer, which is an opposite tendency to that obtained in this study in the upper thermosphere. GWs in Figure 4 show slightly larger amplitudes at higher latitudes in the MSO and GEO coordinates, which are primarily caused by the monotonous increase

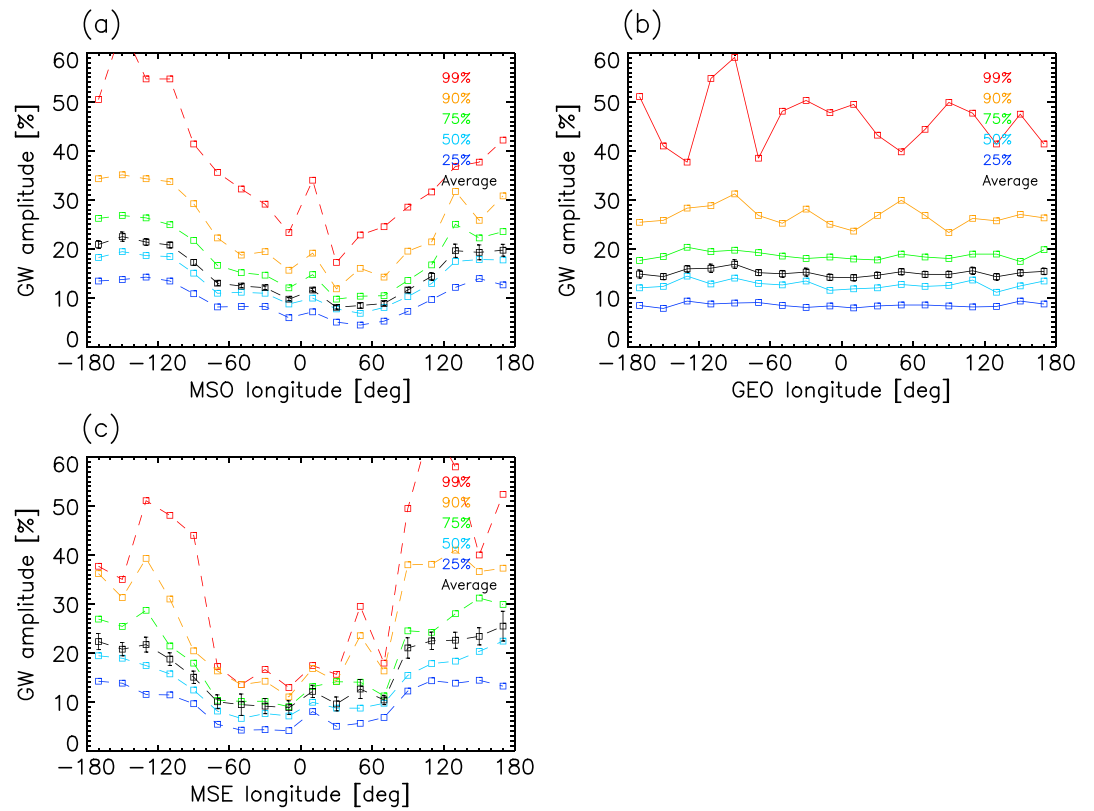


Figure 5. Same as Figures 4a, 4b, and 4c, but as functions of longitude.

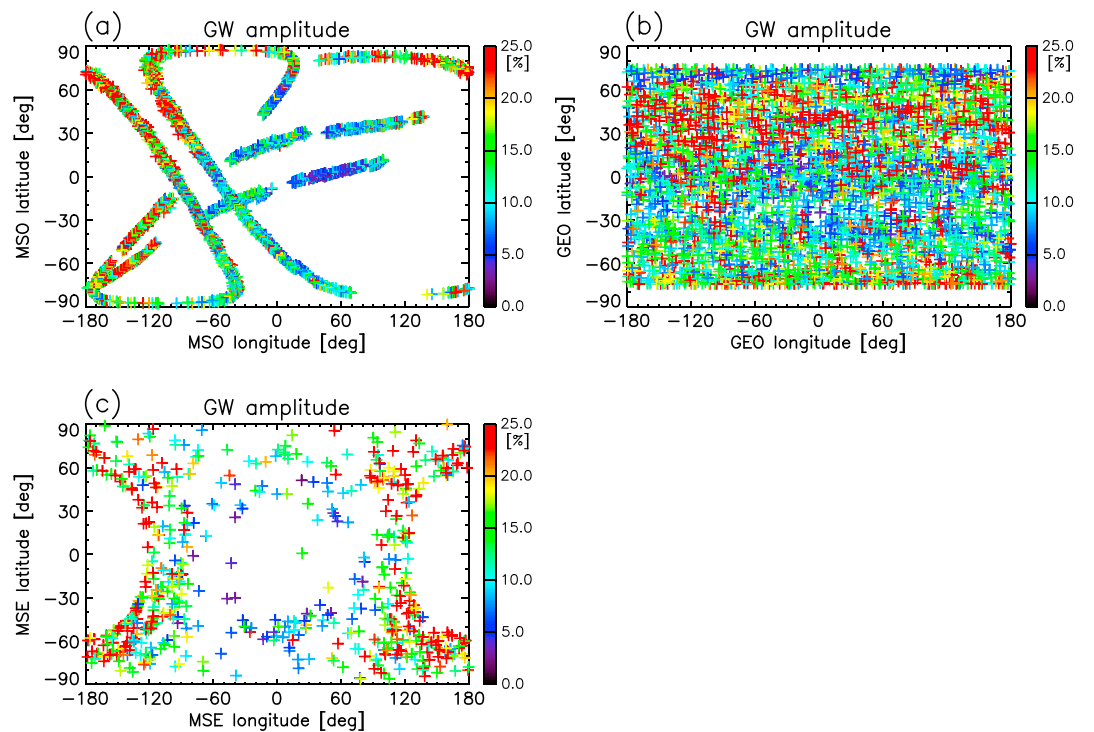


Figure 6. Longitudinal-latitude distributions of the GW amplitudes in the (a) MSO, (b) GEO, and (c) MSE coordinates.

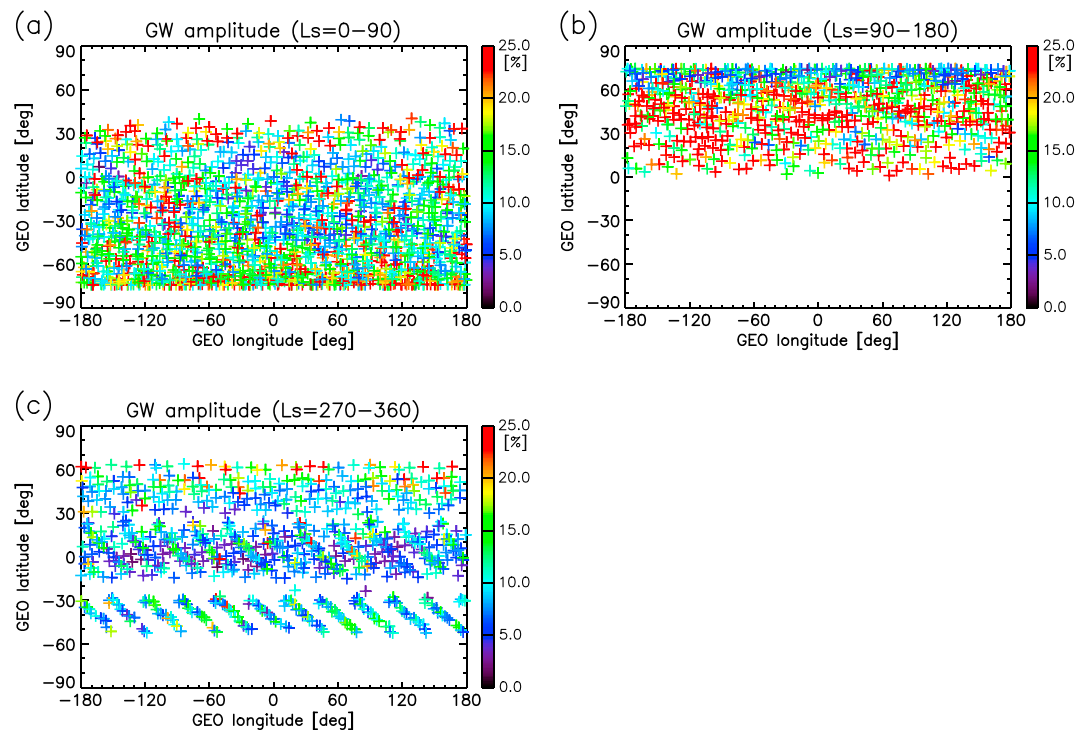


Figure 7. Longitudinal-latitudinal distributions of the GW amplitudes in the GEO coordinate at (a) $L_s = 0^\circ\text{--}90^\circ$, (b) $L_s = 90^\circ\text{--}180^\circ$, and (c) $L_s = 270^\circ\text{--}360^\circ$. Those at $L_s = 180^\circ\text{--}270^\circ$ are not displayed because of no observation during this period.

in the average amplitude with SZA, and these tendencies become less clear when the GW amplitudes are corrected according to the upper thermospheric temperature T_0 (see section 4.4).

Figure 5 illustrates the longitudinal dependences of the GW amplitudes in the MSO, GEO, and MSE coordinates. The average amplitude varies from $\sim 10\%$ on the dayside to $\sim 20\%$ on the nightside in the MSO and MSE coordinates. The longitudinal dependence of the average amplitude and percentile curves in the MSO coordinate are qualitatively similar to that reported from Pioneer Venus Orbiter (PVO)/Neutral Mass Spectrometer (NMS) measurements in the Venusian upper thermosphere [Kasprzak *et al.*, 1988], although a pronounced minimum near -150° MSO longitude is not recognized in the MAVEN/NGIMS data. A quantitative comparison, however, reveals that the GW amplitude in the Martian upper thermosphere is about twice that on Venus: In the Venusian upper thermosphere, the average amplitude is $\sim 5\%$ on the dayside and $\sim 10\%$ on the nightside for the CO_2 density perturbations. Note that when comparing atmospheric perturbations at different planets, we need to compare wave amplitudes at the same mean density level, as suggested by Forbes *et al.* [2006]. In fact, Kasprzak *et al.* [1988] reported that the amplitude of small-scale perturbations increases with altitude in the Venusian upper thermosphere. Our study of Mars investigates the number density level between 10^5 and 10^7 cm^{-3} for Ar, which roughly corresponds to approximately several $10^6\text{--}10^8 \text{ cm}^{-3}$ for the main composition (CO_2 below $\sim 210 \text{ km}$ and O above that altitude on the dayside of Mars [Mahaffy *et al.*, 2015]). This density level is similar to that in the work of Kasprzak *et al.* [1988], although O dominates at that density level on Venus and O/ CO_2 mixing ratio is more than an order of magnitude larger on Venus than on Mars around the exobase [Keating and Bougher, 1992; Bougher, 1995]. Because of the proximity of Venus to the Sun, photodissociation of CO_2 yields O and CO more efficiently, leading to the larger O/ CO_2 ratio in the thermosphere of Venus. This increase in the O density in the Venusian thermosphere causes more efficient radiative cooling in the CO_2 $15 \mu\text{m}$ bands induced primarily through $\text{CO}_2\text{--O}$ collisions. The relatively small amplitude of GWs in the Venusian upper thermosphere may be caused by efficient dissipation of GWs due to the CO_2 $15 \mu\text{m}$ radiative damping, which will be discussed in section 4.2. The longitudinal dependences in the MSO and MSE coordinates in Figures 5a and 5c again become obscure when the GW amplitudes are corrected according to T_0 (section 4.4).

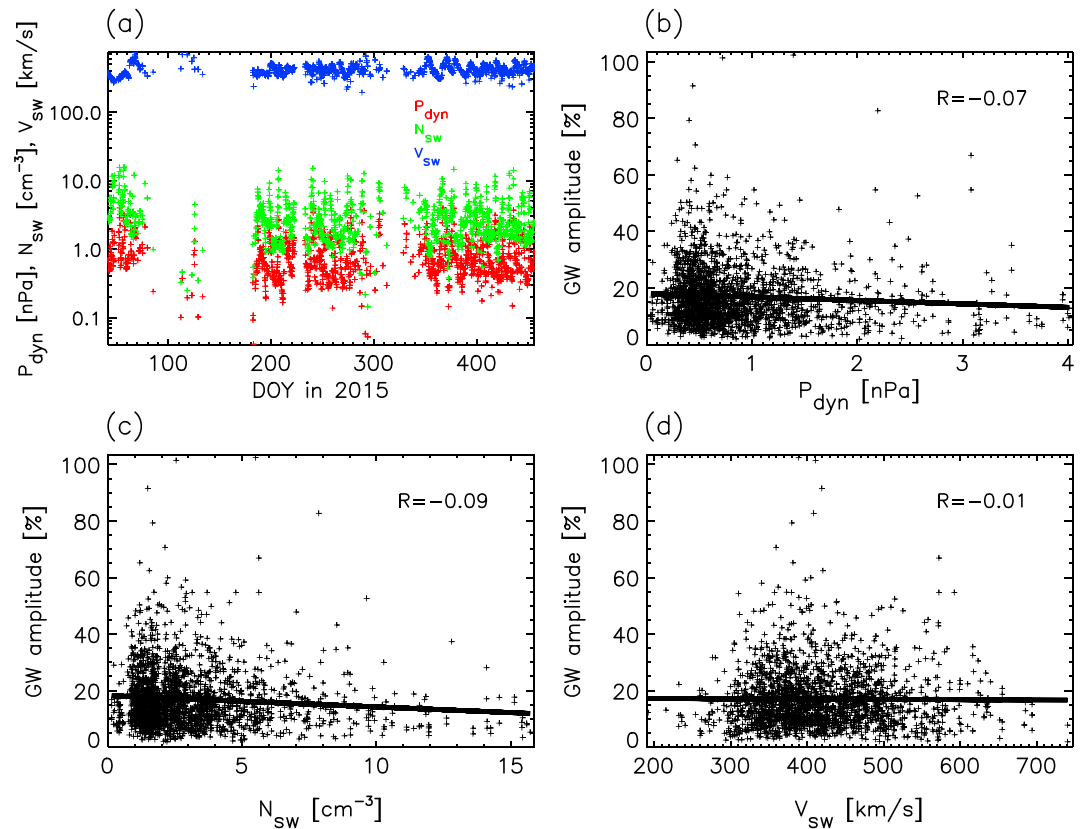


Figure 8. (a) Solar wind dynamic pressure, number density, and velocity measured in the solar wind region from 11 February 2015 to 31 March 2016. The GW amplitudes plotted as a function of (b) solar wind dynamic pressure, (c) solar wind number density, and (d) solar wind velocity. The black plus symbols mark the GW amplitudes, and the black line shows the linear regression line. The correlation coefficient (R) is indicated in each diagram.

We should be cautious when interpreting the latitudinal and longitudinal dependences in the MSO and MSE coordinates in Figures 4a, 4c, 5a, and 5c, because they can be partly caused by the biased data coverage (see the nonuniform longitudinal-latitudinal data coverage in Figures 6a and 6c). For instance, almost no data is available near the subsolar region in the MSE coordinate (Figure 6c), owing to the orbital configuration.

Figure 6 illustrates the longitudinal-latitudinal distributions of the GW amplitudes in the MSO, GEO, and MSE coordinates. In the MSO coordinate (Figure 6a), anticorrelation with the exobase temperature obtained from Martian thermospheric GCMs [e.g., González-Galindo *et al.*, 2009; S. W. Bougher *et al.*, 2015] is recognized; for instance, the dawn-dusk asymmetry near the subsolar region in Figure 6a is well anticorrelated with the modeled exobase temperature. In the GEO coordinate (Figure 6b), we see north-south asymmetry with larger amplitudes in the Northern Hemisphere. However, this asymmetry turns out to be mainly caused by the seasonal and day-night variations (see Figure 7) and becomes less prominent when the amplitudes are corrected according to T_0 (see Figures 12 and 13). Longitudinal dependence in the GEO coordinate (Figure 6b) is unclear, as we can see also in Figure 5b. Possible correspondence between the thermospheric GW activity and Mars' topography such as Tharsis Montes around 15°S–15°N and 90°W–120°W in the GEO coordinate is not clearly identified in this data set. No correspondence to higher orographic variance in the Southern Hemisphere is recognized, consistent with the MGS accelerometer measurements [Creasey *et al.*, 2006b].

Figure 7 shows the seasonal variations of the GW amplitude distributions in the GEO coordinate. $L_s = 180^\circ$ – 270° is not shown because of no observations during this period. Note that some of the apparent seasonal variations in Figure 7 come from the orbital bias of MAVEN. One may notice larger amplitude GWs populate in the middle latitudes in the northern summer (at $L_s = 90^\circ$ – 105°) in Figure 7b and around 30°N (at $L_s = 80^\circ$ – 90°) in Figure 7a. However, these larger amplitude GWs were measured on the nightside (at $> 25^\circ$ latitude and $< -80^\circ$ longitude in the MSO coordinate in Figure 6a (see also inbound segments in

Figures 2e and 2f)), while relatively smaller amplitude GWs at $> 60^\circ$ latitude (at $L_s = 115^\circ\text{--}130^\circ$) in Figure 7b were observed on the dayside (around $45^\circ\text{--}75^\circ$ latitude and $\sim 0^\circ$ longitude in the MSO coordinate in Figure 6a (see inbound segments in Figures 2e and 2f)), indicating that the difference in the GW amplitudes partly reflects the day-night variation. Larger amplitude GWs at $> 50^\circ$ latitude in Figure 7c also come from post-terminator measurements. This orbital bias effect (or bias in the background atmosphere) needs to be removed before examining seasonal variations (section 4.4).

Figure 8 illustrates dependences of the GW amplitudes on the solar wind parameters. Almost no or very weak anticorrelations of the GW amplitudes with solar wind dynamic pressure and density are observed. The GW amplitudes tend to be slightly smaller with increasing solar wind dynamic pressure and density. However, these dependences are not larger than a few percent, playing a less important role in determining the GW amplitudes.

4. Discussion

The GW amplitudes around the Martian exobase appear to have a clear dependence on the background temperature (T_0) of the upper thermosphere. They also depend on SZA, solar EUV irradiances, and latitudes and longitudes in various coordinate systems. However, these parameters are not independent variables, i.e., some of the dependences can be indirectly caused by the others. In this section, we first discuss possible physical basis of the T_0 dependence, and then attempt to remove it from the GW amplitudes to obtain “corrected GW amplitudes.” The other parameter dependences are reanalyzed using the corrected GW amplitudes.

4.1. Physical Basis of the Background Temperature Dependence

The anticorrelation of the GW amplitudes with the scale height (or equivalently, with T_0) of the Martian upper thermosphere was already pointed out by *Yigit et al.* [2015b] using NGIMS data obtained in the morning sector in December 2014. *Yigit et al.* [2015b] attributed this anticorrelation to the effect of vertical advection, which is inversely proportional to the scale height [Del Genio et al., 1979]. *England et al.* [2016] recently showed that the slope of the power spectral densities of $\rho'/\bar{\rho}$ obtained from NGIMS data changes around the apparent wavelengths of ~ 200 km, suggesting that wave dissipation and breaking/saturation tend to preferentially damp shorter wavelength modes as they propagate upwards through the atmosphere [Fritts and Alexander, 2003, and references therein].

We consider that the anticorrelation of the GW amplitudes with T_0 obtained from our statistical study with a larger data set is primarily caused by breaking/saturation of GWs due to convective instability. The theoretical threshold for the breaking/saturation of a monochromatic GW due to convective instability is given as [Smith et al., 1987]

$$u' > |c - u_0|, \tag{1}$$

where u' is the horizontal perturbation velocity, u_0 is the horizontal mean flow velocity, and c is the horizontal phase speed of the wave. Breaking/saturation due to shear instability is neglected here, since it has a higher threshold for a wave having intrinsic frequency much higher than the inertial frequency [Fritts and Rastogi, 1985]. Using equation (1) and the polarization relations for nondissipative GWs [Hines, 1960], we obtain the corresponding threshold of convective instability for the perturbation number density N' as

$$\frac{N'}{N_0} > \left| \frac{\omega_1^2(k_z - i/2H) + i(\gamma - 1)gk_x^2}{\omega_1(\gamma k_z + i(\gamma - 2)/2H)Hgk_x} \cdot \frac{\omega_1}{k_x} \right|, \tag{2}$$

where N_0 is the mean number density, i is the imaginary unit, k_x and k_z are the horizontal and vertical wave numbers, respectively, $\omega_1 = k_x(c - u_0)$ is the intrinsic frequency of the wave, γ is the heat capacity ratio, g is the gravity of the planet, $H = k_B T_0 / mg$ is the scale height, k_B is the Boltzmann constant, T_0 is the mean temperature, and m is the molecular weight of the gas. For simplicity, we assume that Ar behaves similarly to the main composition (CO_2); hence, small differences in wave amplitude and phase between Ar and CO_2 [England et al., 2016] are neglected. The solutions of equation (2) calculated with Mars' parameters of $g = 3.7 \text{ m/s}^2$ and $m = 44 \text{ amu}$ are displayed in Figure 2d with green solid, green dashed, violet solid, and violet solid

curves for a set of horizontal (λ_x) and vertical (λ_z) wavelengths of (λ_x, λ_z) = (>20 km, 20 km), (>40 km, 40 km), (200 km, 200 km), and (400 km, 200 km), respectively. Those curves obtained assuming $\gamma = 5/3$ are indicated with triangles and $\gamma = 1.3$ with squares. Although the main atmospheric component of Mars is CO₂ ($\gamma = 1.3$) around or below the exobase, the O/CO₂ ratio is subject to seasonal, geographical, and temporal variability, so that under some conditions O ($\gamma = 5/3$) becomes dominant. We consider that the threshold is somewhere between curves with squares ($\gamma = 1.3$) and triangles ($\gamma = 5/3$). Note that equation (2) is less sensitive to λ_x , as long as $\lambda_x > \lambda_z$ and $2\pi H > \lambda_z$ are satisfied. The typical apparent wavelengths of the wavelike structures obtained by the NGIMS measurements are 200–400 km around the exobase, which correspond to $\lambda_z = 20$ –40 km ($\lambda_x = 200$ –400 km) if we assume that the observed structures are due to vertical (horizontal) variations. First, we assume that the observed structures are due to vertical rather than horizontal variations, i.e., $\lambda_x > 10\lambda_z$. In this case, the threshold given by equation (2) is approximated using the well-known nondissipative GW dispersion relation in Hines [1960] as

$$\frac{N'}{N_0} > \left| \frac{i(\gamma - 1)gk_x^2}{\omega_1 \gamma k_z H g k_x} \cdot \frac{\omega_1}{k_x} \right| = \frac{\gamma - 1}{\gamma} \frac{mg}{k_B T_0} \left| \frac{1}{k_z} \right| \quad (3)$$

in the short vertical wavelength limit of $|k_z| \gg > 1/H$, $|k_z| \gg > |k_x|$, and $C_s \gg > |\omega_1/k_z|$, where $C_s = \sqrt{\gamma g H}$ is the sound speed. Equation (3) indicates that the threshold for N' is inversely proportional to T_0 in this limit. This approximation is valid for $T_0 > \sim 150$ K when $\lambda_z = 20$ –40 km, for which $|k_z| \gg > 1/H$ is satisfied and equation (3) yields an error less than 10%. Figure 2d shows that a large part of the GWs distribute around the threshold curves obtained for $\lambda_z = 20$ –40 km, suggesting that their amplitudes are limited by the convective breakdown/saturation for moderately long vertical wavelength modes of $\lambda_z = 20$ –40 km.

However, some parts of the GWs distribute above the threshold curves for $\lambda_z = 20$ –40 km. These large amplitude waves would be better explained by longer vertical wavelength modes ($\lambda_z < 100$ –200 km). It is worth noting that in the Earth thermosphere, the dominant vertical wavelength increases exponentially with altitude, and it reaches 150–200 km above 200 km altitude [Oliver *et al.*, 1997; Vadas, 2007; Miyoshi and Fujiwara, 2009]. This is mainly because GWs with longer λ_z are less affected by dissipation and, thus, can propagate to higher altitudes [Yigit *et al.*, 2008]. In the Martian upper thermosphere, England *et al.* [2016] pointed out that the best fit λ_z obtained from a linear two-fluid model ranges from 150 km to 190 km. In this long λ_z case, the observed apparent wavelengths of 200 ~ 400 km require horizontal variations with $\lambda_x = 200$ –400 km. Assuming that the observed structures are due to horizontal variations, i.e., $\lambda_x < 10\lambda_z$, the GW amplitude threshold given by equation (2) is approximated as

$$\frac{N'}{N_0} > \frac{\gamma \left(1 + \frac{1}{4H^2 k_x^2} \right) \left(1 - \sqrt{1 - \frac{4(\gamma-1)}{\gamma^2 (H|k_x| + (4H|k_x|)^{-1})^2}} \right) - 4(\gamma-1)}{2(2-\gamma)} \quad (4)$$

in the long vertical wavelength limit of $|k_z| \ll < 1/H$. Equation (4) indicates that the threshold again anticorrelates with T_0 , which is depicted in Figure 2d with violet solid and dashed curves. In addition to T_0 , equation (4) depends also on k_x . The threshold given by equation (4) (hence equation (2)) asymptotes to

$$\frac{N'}{N_0} > \frac{2(\gamma-1)}{\gamma} = \begin{cases} 0.46 & \text{for } \gamma = 1.3, \\ 0.80 & \text{for } \gamma = 5/3 \end{cases} \quad (5)$$

in the long vertical and horizontal wavelength limit of $|k_z| \ll < 1/H$ and $|k_x| \ll < 1/H$. Equation (5) gives the upper limit on any monochromatic GW amplitude. The T_0 dependence in Figure 2d suggests that the GW amplitude is primarily determined by convective breaking/saturation in part for moderately long vertical wavelength modes ($\lambda_z = 20$ –40 km), while some of the large amplitude waves favor very long vertical wavelength modes ($\lambda_z < 100$ –200 km). This consideration qualitatively explains the observed distribution of GW amplitudes in the upper thermosphere. The role of other GW damping processes (molecular diffusion, radiative damping, and ion drag) in comparison to convective instabilities is yet to be established for the Martian upper thermosphere.

Table 2. Theoretical Thresholds for the Breaking/Saturation Due to Convective Instability Calculated From Equation (2) and the Average GW Amplitudes Observed Around the Exobases of Mars, Venus, and Earth^a

	T_0 (K)	g (m/s ²)	m (amu)	γ (#)	λ_z (km)	Threshold Due to Convective Instability (equation (2))	Observed Average GW Amplitude
Mars dayside	270	3.7	44	1.3	30	7.9%	~10%
Mars dayside	270	3.7	44	5/3	30	14%	
Mars dayside (long λ_z)	270	3.7	44	1.3	150	28%	
Mars dayside (long λ_z)	270	3.7	44	5/3	150	52%	
Mars nightside	160	3.7	44	1.3	30	13%	~20%
Mars nightside	160	3.7	44	5/3	30	22%	
Mars nightside (long λ_z)	160	3.7	44	1.3	150	35%	
Mars nightside (long λ_z)	160	3.7	44	5/3	150	64%	
Venus dayside	270	8.9	44	5/3	30	31%	~5%
Venus dayside (long λ_z)	270	8.9	44	5/3	150	71%	
Venus nightside	100	8.9	44	5/3	30	60%	~10%
Venus nightside (long λ_z)	100	8.9	44	5/3	150	78%	
Earth dayside (low latitude)	1200	9.8	16	5/3	150	15%	~1%
Earth nightside (low latitude)	900	9.8	16	5/3	150	19%	~1.5%
Earth polar region (high latitude, quiet period: Kp index ~ 0)	1100	9.8	16	5/3	150	16%	~3%
Earth polar region (high latitude, disturbed period: Kp index $> \sim 7$)	1100	9.8	16	5/3	150	16%	~8%

^aParameters are based on *Bougher et al.* [1999] for the upper thermospheric temperatures (T_0), gravity (g), molecular weight (m), and heat capacity ratio (γ), and on *Oliver et al.* [1997] and *Miyoshi and Fujiwara* [2009] for the vertical wavelength (λ_z) of GWs in the terrestrial upper thermosphere. $\lambda_x > \lambda_z$ is assumed in calculating the theoretical thresholds from equation (2). The average GW amplitudes observed around the exobase of Venus are taken from *Kasprzak et al.* [1988], and those of Earth are taken from the medium-scale ($\lambda_x = 160 - 600$ km) density perturbations observed in the 370 - 450 km altitude range in *Bruinsma and Forbes* [2008].

A theoretical work by *Eckermann et al.* [2011] estimated the relative importance of the GW damping processes on Mars assuming a windless atmosphere. They estimated that wave saturation becomes the dominant flux deposition mechanism at high altitudes for long vertical wavelength modes ($\lambda_z > 15$ km). For instance, more than 90% of the GW momentum flux is dissipated by saturation and less than 10% by radiative damping above 100 km for a GW harmonic with $\lambda_z = 40$ km, before the harmonic is rapidly damped by molecular diffusion at higher altitudes. Our result in Figure 2d is consistent with the estimates of *Eckermann et al.* [2011] in that the wave saturation is the dominant process to determine the GW amplitude in the Martian thermosphere.

On the other hand, the CO₂ 15 μ m radiative damping and molecular viscosity are also functions of the background temperature T_0 . According to equations (13) and (21) in *Eckermann et al.* [2011], the damping rates due to the CO₂ 15 μ m radiative damping and molecular viscosity increase with T_0 by factors of 95 and 3, respectively, over the temperature range considered here ($T_0 = 100 - 350$ K). Although the radiative damping would be of minor importance around the exobase of Mars, it may play a more important role in the Venusian upper thermosphere in generating day-night variations of GW amplitudes, because the CO₂ 15 μ m radiative cooling is relatively more efficient on Venus, as discussed in section 3.

4.2. Comparisons With Observed Amplitudes on Mars, Venus, and Earth

Table 2 summarizes the theoretical thresholds for the breaking/saturation due to convective instability calculated from equation (2) and their comparisons with the average GW amplitudes observed around the exobases of Mars, Venus, and Earth. The convective instability thresholds for Mars are calculated based on the parameters from the work of *Bougher et al.* [1999] assuming either CO₂ gas ($\gamma = 1.3$) or O gas ($\gamma = 5/3$). In contrast, O dominates around the exobases at Venus and Earth [e.g., *Bougher et al.*, 1999]; therefore, an ideal monoatomic gas ($\gamma = 5/3$) is assumed for these planets. The average GW amplitudes observed around the exobase of Venus are taken from the PVO/NMS observations in *Kasprzak et al.* [1988], and those for Earth are taken from the medium-scale ($\lambda_x = 160 - 600$ km) density perturbations observed by CHAMP/STAR both in the low-latitude and polar regions in Figure 6 of *Bruinsma and Forbes* [2008]. The low-latitude region of the terrestrial upper thermosphere is less affected by the energy deposition from the magnetosphere,

whereas the wave activity in the polar region exhibits a clear dependence on the magnetospheric activity. Therefore, the observed wave amplitudes in the terrestrial polar regions are shown both for magnetically quiet (Kp index ~ 0) and disturbed periods (Kp index $> \sim 7$). In Table 2, we see that the instability thresholds for Venus are significantly larger than those for Mars, mainly because of the larger gravity. However, the observed GW amplitudes in the Venusian upper thermosphere are about a half of those on Mars both on the dayside and nightside. This difference between Venus and Mars can possibly be explained by different efficiencies of the CO_2 $15\ \mu\text{m}$ radiative damping. GWs are attenuated by the radiative damping far below the convective instability threshold in the Venusian upper thermosphere because of the larger O/CO_2 ratio, whereas the radiative damping plays a minor role in the Martian upper thermosphere for long vertical wavelength modes ($\lambda_z > \sim 15\ \text{km}$) [Eckermann *et al.*, 2011]. Our consideration excludes sources of GWs, which may be weaker on Venus.

Comparing Mars and the low-latitude region of Earth, we find that the observed GW amplitudes are more than 10 times smaller on the latter than on the former. This difference is qualitatively consistent with, but quantitatively larger than, the amplitude difference for the longer period (~ 27 days) perturbations presented by Forbes *et al.* [2006]. There, the response of the upper thermospheric density to the 27 day solar flux variations ($\Delta\rho/\Delta F$) was about twice smaller on Earth than on Mars. The larger difference between Earth and Mars that follows from our study can be attributed to stronger dissipation of short period (approximately tens of minutes) perturbations on Earth or stronger sources of GWs on Mars. The former can be related to the significant ion drag and molecular diffusion on Earth, which would attenuate GWs below the instability threshold in the terrestrial thermosphere [Yigit *et al.*, 2008]. The latter includes sources below, upward propagation of GWs in the lower and middle atmosphere, and source above, including in situ excitation of GWs in the thermosphere by solar wind forcing. For GW sources below, a poleward shift of the peak of GW energy with increasing altitude, which was found both on Earth [Sato *et al.*, 2009; Yigit *et al.*, 2009; Miyoshi *et al.*, 2014] and Mars [Medvedev *et al.*, 2011b; Miyoshi *et al.*, 2011; Kuroda *et al.*, 2015], diminishes the relative GW activity in the low-latitude thermosphere.

For GW sources above, the situation is quite different on Earth and Mars, because Mars (and Venus) has no planetary-scale magnetic field like Earth. In the polar regions of Earth, in situ excitation of thermospheric disturbances by the energy deposition from the magnetosphere dominates over the contribution from below. We see in Table 2 that the average GW amplitude increases to $\sim 8\%$ during disturbed periods (or 12–15%, if longer wavelength modes are taken into account [Bruinsma and Forbes, 2008]), which is closer to the convective instability threshold of 16% for a monochromatic GW obtained from equation (2). This enhancement indicates that the in situ GW excitation by the magnetospheric energy deposition is capable of generating large-amplitude perturbations in the upper thermosphere. On Earth, magnetospheric energy is deposited into the auroral region mainly in the form of Joule heating and particle precipitations [Knipp *et al.*, 2004]. On the other hand, pickup oxygen ions precipitating into the atmosphere can be a strong heat source in the upper thermospheres of Mars and Venus [Luhmann and Kozyra, 1991; Leblanc and Johnson, 2002; Chaufray *et al.*, 2007; Fang *et al.*, 2013]. Fang *et al.* [2013] estimated that the temperature perturbations in the Martian upper thermosphere due to the precipitating O^+ can be up to $\sim 3\%$ for a quiet condition, $\sim 7\%$ for an active condition, and $\sim 155\%$ for an extreme condition, although they assumed a 100% heating efficiency when calculating these temperature disturbances, and a more elaborate method like Direct Simulation Monte Carlo (DSMC) modeling [Terada *et al.*, 2016] is needed to obtain a realistic heating efficiency. This O^+ precipitation may represent a unique in situ GW generation process in the Martian and Venusian thermospheres and will be discussed in section 4.5.

4.3. Corrected Gravity Wave Amplitudes

The linear regression line between the GW amplitudes and T_0 (black line in Figure 2d) is used to obtain the corrected GW amplitudes. Namely, the corrected GW amplitude a'_i is obtained from

$$a'_i = a_i \frac{y(T_{\text{ave}})}{y(T_i)}, \quad (6)$$

where a_i is the GW amplitude before correction, $y(T_i)$ is the linear regression line in Figure 2d as a function of temperature, T_{ave} is the average temperature, T_i is the temperature obtained from Step 1 in section 2 for respective profiles, and subscript i runs for all profiles. Although SZA has a similar correlation strength to T_0 (Table 1), the linear regression line for T_0 is used here because a possible physical relationship between a_i

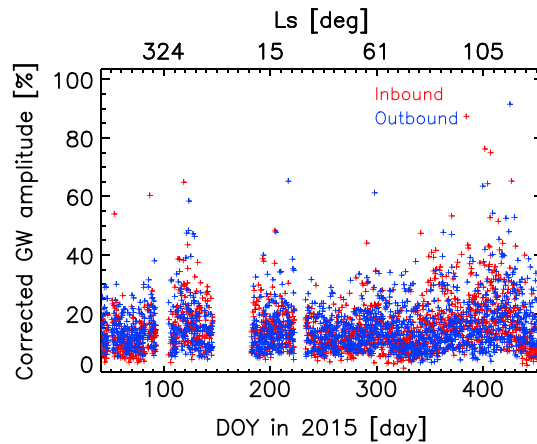


Figure 9. Corrected GW amplitudes from 11 February 2015 to 31 March 2016. The red and blue plus symbols indicate the corrected GW amplitudes for inbound and outbound legs, respectively.

and T_i is suggested by *Yigit et al.* [2015b] and in the discussion in section 4.1. Note that even if we use the linear regression line between a_i and SZA instead of that between a_i and T_0 , most of the results presented here do not change. Figure 9 shows the corrected GW amplitudes obtained from equation (6). Some of the middle- to long-term variations observed in Figure 2 are removed by the correction, while ~20% of short-term variations still remain.

4.4. Parameter Dependences of the Corrected Gravity Wave Amplitudes

Figure 10 illustrates the latitudinal and SZA dependences of the corrected GW amplitudes. Comparing Figure 10 with Figure 4, we see that the positive slope in the SZA dependence is diminished by the correction using equation (6), reflecting a strong anticorrelation between T_0 and SZA (correlation coefficient between T_0 and SZA is -0.77). However, a bump appears at $SZA < 40^\circ$ after the correction, possibly resulting from the dawn-dusk asymmetry near the subsolar region discussed in Figure 6a. The latitudinal dependences in the MSO and GEO coordinates become less prominent after the correction, indicating that the major part of the latitudinal dependences in Figure 4 come from the latitudinal variation in the upper thermospheric temperature T_0 . However, there still remains a very weak latitudinal dependence in Figures 10a and 10b, i.e., very weak

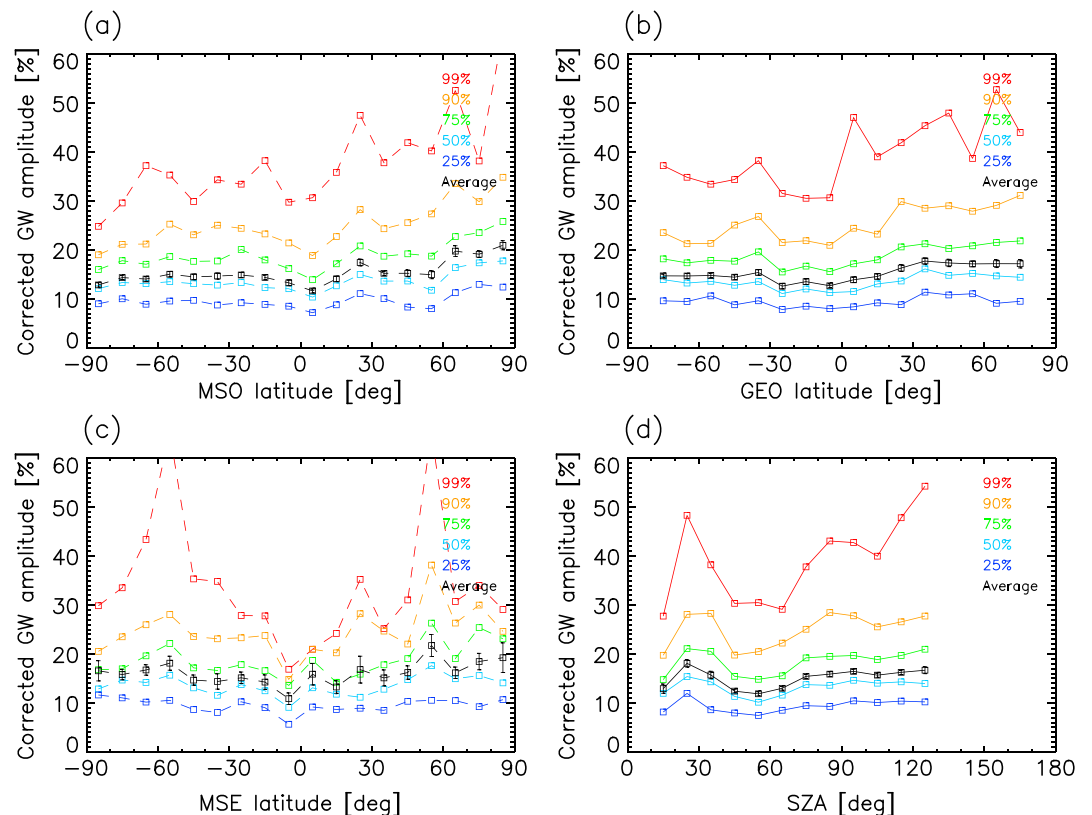


Figure 10. Same plot as Figure 4 but for the corrected GW amplitudes.

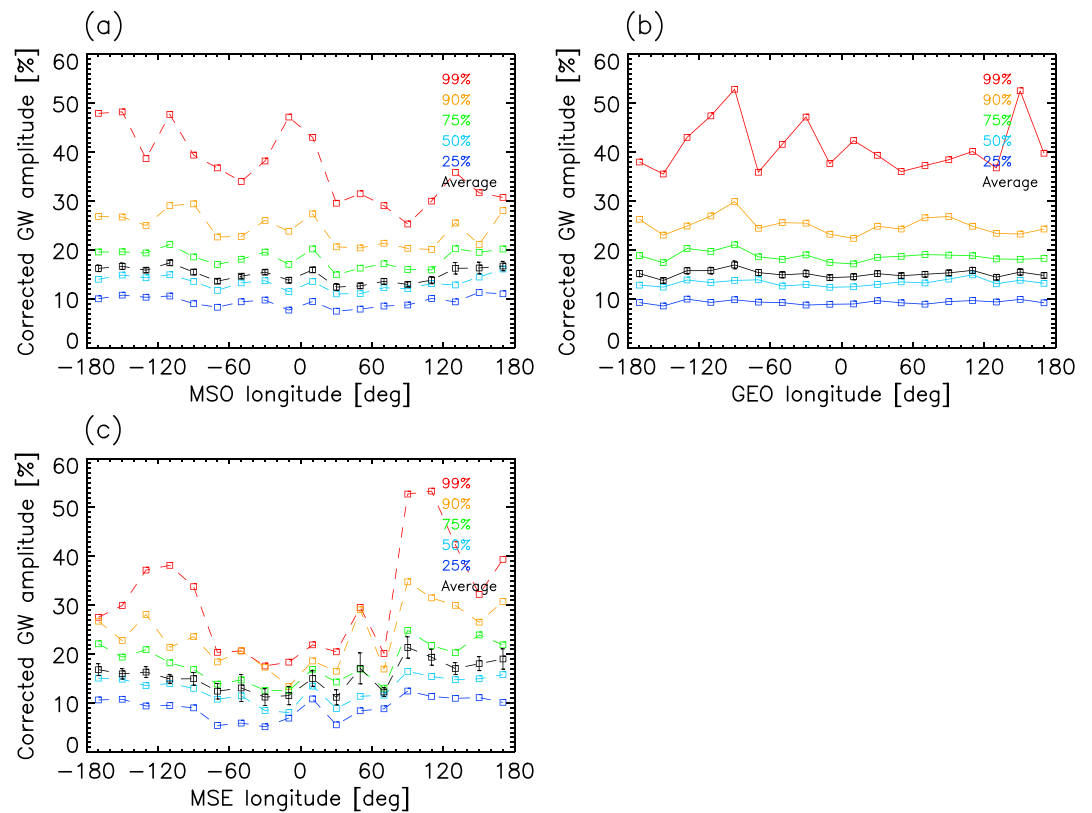


Figure 11. Same plot as Figure 5 but for the corrected GW amplitudes.

north-south asymmetry with slightly larger amplitudes in the Northern Hemisphere and a very subtle dip near the equator in the MSO and GEO coordinates. The larger amplitudes in the Northern Hemisphere are consistent with the MGS accelerometer measurements in the lower thermosphere [Creasey *et al.*, 2006b], indicating no clear connection between the thermospheric wave activity and the topography of Mars, since the Southern Hemisphere has higher orographic variance and should have higher wave activity if they are connected. It is worth noting that Creasey *et al.* [2006b] found that the amplitude variance in the Northern Hemisphere during northern winter ($L_s = 286^\circ - 300^\circ$) was about 50% larger than that in the Southern Hemisphere during southern winter ($L_s = 84^\circ - 86^\circ$). This latitudinal contrast would further increase in Creasey *et al.* [2006b] if the amplitudes were corrected by temperature, because temperatures should be higher during northern winter than during southern winter, indicating that the difference in the latitudinal contrast between the lower thermosphere [Creasey *et al.*, 2006b] and the upper thermosphere (this study) would be much larger. Note also that an enhancement in the amplitude variance in the Northern Hemisphere during northern winter in Creasey *et al.* [2006b] is consistent with a recent high-resolution Martian GCM [Kuroda *et al.*, 2016], but it is not clearly recognized in Figure 13c of this study. Considering that there also exists the opposite tendency in day-night asymmetry between the lower and upper thermospheres as noted in Section 3, there may be a large difference in the nature of GWs between these regions. Figure 11 shows the longitudinal dependences of the corrected GW amplitudes. The day-night asymmetry in the MSO coordinate (Figure 5a) similar to that observed in the Venusian upper thermosphere [Kasprzak *et al.*, 1988] becomes obscure after the correction. No clear longitudinal dependence is found in the GEO coordinate, indicating negligible influence from Mars' topography. Figure 12 shows the longitudinal-latitudinal distributions of the corrected GW amplitudes. In the MSO and MSE coordinates, the day-night variation becomes less clear, but some inhomogeneity is still recognized after the correction. In the GEO coordinate, the corrected GW amplitudes have slightly smaller values around the equator region and Southern Hemisphere as seen in Figure 10b.

These very weak latitudinal dependences (slightly smaller amplitudes around the equator and Southern Hemisphere) recognized in Figures 10a, 10b, 12a, and 12b may be caused by (1) latitudinal dependence of

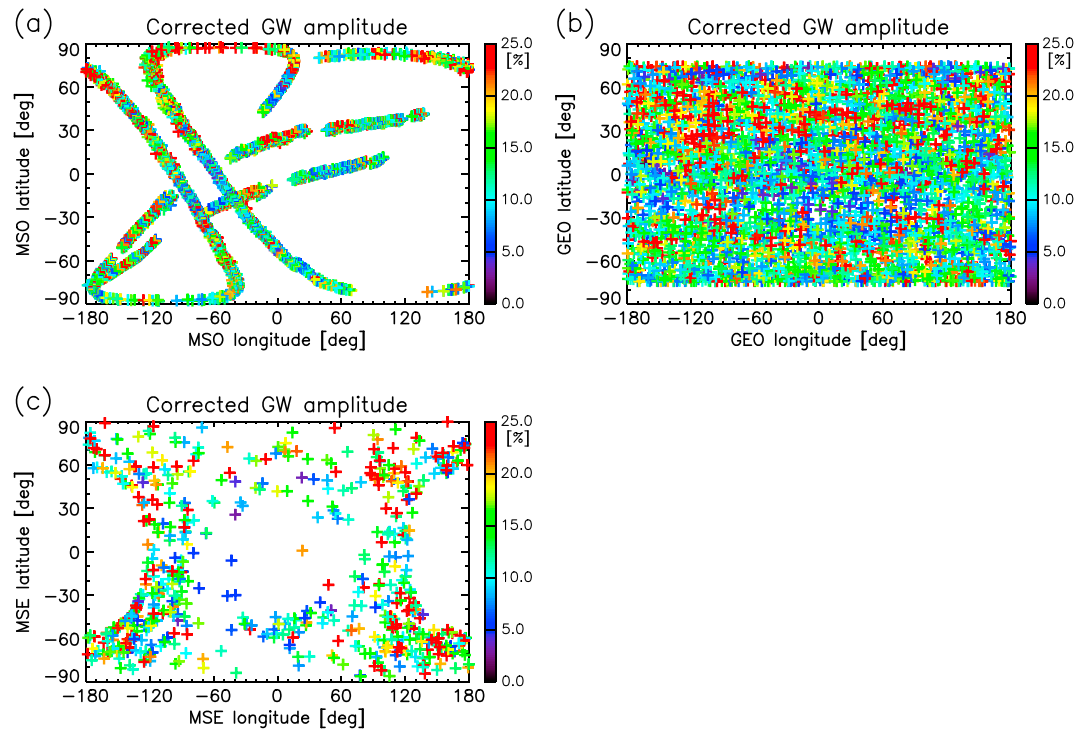


Figure 12. Same plot as Figure 6 but for the corrected GW amplitudes.

GWs propagating from the lower and middle atmosphere or (2) ion drag in the thermosphere around magnetic anomalies. The tendency of larger GW amplitudes at high latitudes in the thermosphere is consistent with GCMs [e.g., Miyoshi *et al.*, 2011; Medvedev *et al.*, 2011b], although much larger latitudinal variation (a factor of 2 or more) is expected from GCMs. The ion drag might be strong enough to cause dissipation of GWs around the magnetic anomalies especially in the Southern Hemisphere and equatorial region [Connerney *et al.*, 2001, 2015], since the magnetic field strength around the strong anomalies reaches ~ 1600 nT around 100 km altitude [Acuña *et al.*, 1999]. However, the correspondence between the map of the magnetic anomalies and Figure 12b is so vague that we cannot draw a definite conclusion at this stage.

Seasonal variation is one of the key issues in identifying the possible connection between the upper thermosphere and the lower and middle atmosphere. Comparing Figures 7 and 13, we find that the seasonal variation of the average GW amplitude in the upper thermosphere is diminished from a factor of ~ 2 (in Figure 7, the average amplitude is 15.4% for $L_s = 0^\circ - 90^\circ$, 19.6% for $L_s = 90^\circ - 180^\circ$, and 9.7% for $L_s = 270^\circ - 360^\circ$) to ~ 1.3 (in Figure 13, the average amplitude is 14.1% for $L_s = 0^\circ - 90^\circ$, 17.9% for $L_s = 90^\circ - 180^\circ$, and 14.6% for $L_s = 270^\circ - 360^\circ$) after the correction, which is reasonably explained by the seasonal variation in the exospheric temperature [e.g., S. W. Bougher *et al.*, 2015]. Although the seasonal variation in the GW amplitudes becomes less clear after the correction, there still remain slightly elevated amplitudes at middle latitudes in the northern summer ($L_s = 90^\circ - 180^\circ$ in Figure 13b). Miyoshi *et al.* [2011] analyzed GW activity in the northern summer using a GCM and found that the GW activity in the northern middle latitudes ($40^\circ\text{N} - 60^\circ\text{N}$) around 110 km altitude is enhanced by breaking and dissipation of diurnal and semidiurnal tides. The larger amplitudes in the northern middle latitudes in Figure 13b might be interpreted following this scenario, but obviously we need more data in low latitudes and Southern Hemisphere in Figure 13b before drawing any conclusion on the latitudinal dependence of the corrected amplitudes at a specific season.

Figure 14 displays the altitude variations of the absolute value of the relative density perturbations $|N - N_{\text{fit}}|/N_{\text{fit}}$ and those corrected by temperature. The average amplitude increases by 40–50% both on the dayside and nightside from the altitude where $N(\text{Ar}) = 10^7 \text{ cm}^{-3}$ to the altitude where $N(\text{Ar}) = 10^5 \text{ cm}^{-3}$, indicating 9–11% increase per scale height. Contrary to Figure 2 in Yiğit *et al.* [2015b], the average

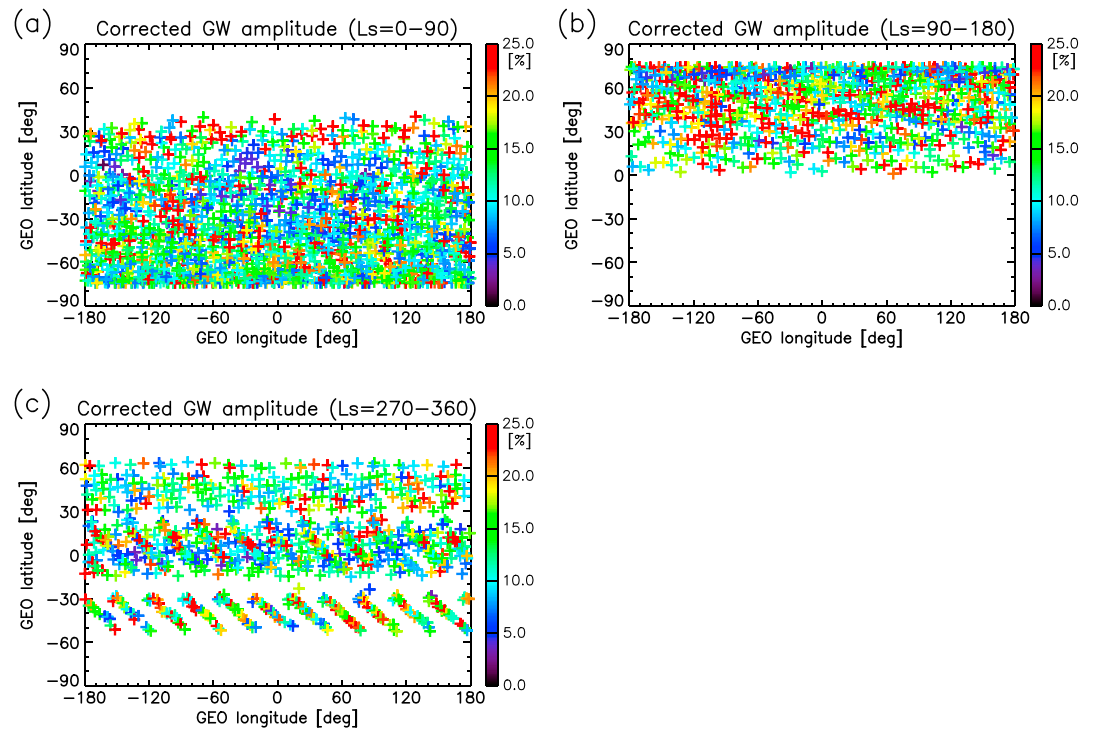


Figure 13. Same plot as Figure 7 but for the corrected GW amplitudes.

amplitudes keep increasing up to the upper altitude limit. This result suggests that the exponential amplitude growth dominates over dissipation even around the exobase of Mars.

Table 3 summarizes the correlation coefficients after the correction. Comparing Tables 1 and 3, we find that the correlation coefficients between the EUV irradiances and the GW amplitudes are diminished by an order of magnitude after the correction. In contrast, those between the solar wind parameters and the GW amplitudes do not systematically change. This difference suggests that the solar EUV flux controls GW amplitudes through T_0 , whereas solar wind effects (if exist) are irrelevant to T_0 .

4.5. Possible Sources of GWs in the Martian Upper Thermosphere

As discussed in section 4.2, GW activity in the upper thermosphere is significantly elevated on Mars compared to those on Venus and Earth. This difference can be attributed to the differences in dissipation processes and/or sources of GWs. In this section, possible sources of GWs in the Martian upper thermosphere are discussed. Thermospheric GWs consist, generally, of harmonics propagating from the lower and middle atmosphere and those locally excited by the solar wind forcing. We find little evidence for longitudinal variability in Figures 5b, 6b, 11b, and 12b, which would indicate less connection between the upper thermospheric GWs and specific topography features. On the other hand, a very weak latitudinal variability (slightly weaker activity at low latitudes) is recognized in Figures 4b, 6b, 10b, and 12b, which is reminiscent of the poleward shift of the GW energy peak with increasing altitude simulated by GCMs for Earth [e.g., Sato et al., 2009; Yiğit et al., 2009; Miyoshi et al., 2014] and Mars [Medvedev et al., 2011b; Miyoshi et al., 2011; Kuroda et al., 2015, 2016]. Although the latitudinal variation is quantitatively smaller in these figures compared to that in GCMs, it may result from neglecting the seasonal variability. We should, however, note that no clear latitudinal variability is observed at specific seasons in Figure 13. Another problem of the upward propagating GWs is that those with a short vertical wavelength of $\lambda_z < \sim 20$ km would dissipate below 100–120 km. Only those with a very long vertical wavelength of $\lambda_z = 50$ –100 km can reach altitudes up to 150–250 km [Imamura et al., 2016], where MAVEN/NGIMS measured large amplitude GWs.

Concerning GW sources above, in situ excitation of thermospheric disturbances may occur by precipitating ions (pickup ions and solar wind ions) due to the lack of a planetary-scale magnetic field on Mars (and

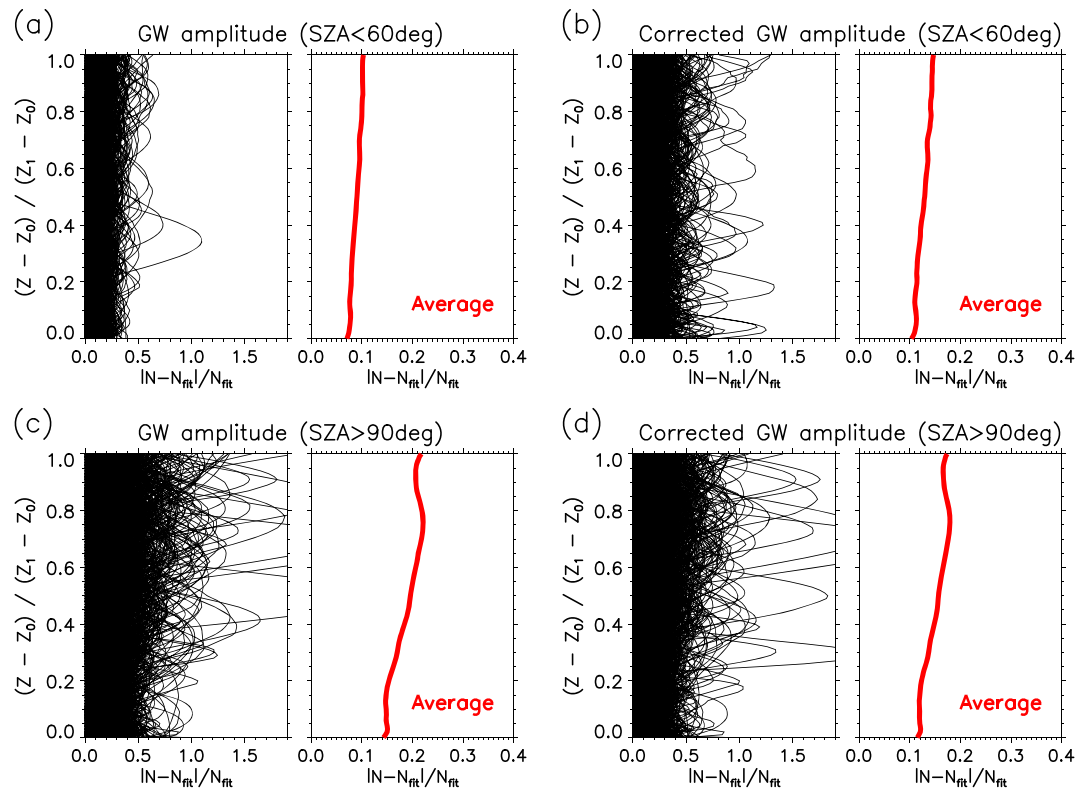


Figure 14. Left panels show the altitude profiles of the absolute value of (a) relative density perturbations for 888 profiles on the dayside at SZA < 60°, (b) corrected relative density perturbations for 888 profiles on the dayside at SZA < 60°, (c) relative density perturbations for 1394 profiles on the nightside at SZA > 90°, and (d) corrected relative density perturbations for 1394 profiles on the nightside at SZA > 90°. Right panels show their averages. z_0 is the altitude where $N(\text{Ar}) = 10^7 \text{ cm}^{-3}$, which roughly corresponds to the exobase for hot O, and z_1 is the altitude where $N(\text{Ar}) = 10^5 \text{ cm}^{-3}$, which roughly corresponds to just above the exobase for Ar and CO_2 .

Venus). Although the energy deposition from precipitating O^+ ions on Mars is about 3 orders of magnitude smaller than the magnetospheric energy deposition of $\sim 100 \text{ GW}$ into the Earth polar thermosphere [Knipp *et al.*, 2004], the precipitating O^+ ions deposit most of their energy at higher altitudes of Mars (above 140 km altitude) [Luhmann and Kozyra, 1991; Fang *et al.*, 2013] than Sun’s EUV flux (below 140 km altitude) [e.g., Fox and Dalgarno, 1979]; hence, the precipitating O^+ ions potentially have a competing effect in the Martian upper thermosphere against the solar EUV energy flux. According to the estimates in Fang *et al.* [2013], thermospheric perturbations have larger amplitudes in the 200–250 km altitude range. Localized perturbations are generated both on the dayside and in the post-terminator region, and they are transported by horizontal winds in the thermosphere. The spatial distribution of the energy deposition from the precipitating O^+ ions is expected to have a distinct asymmetry in the direction of the solar wind motional electric field [Luhmann and Kozyra, 1991; Leblanc and Johnson, 2002; Chaufray *et al.*, 2007; Fang *et al.*, 2013], which is highly variable associated with changes in the IMF clock angle and solar wind velocity. One would expect this asymmetry to be observed as a north-south asymmetry in the MSE coordinate. However, no clear north-south asymmetry is found in Figures 4c, 6c, 10c, and 12c obtained from MAVEN/NGIMS measurements. It might be due to horizontal transport of perturbations and their temporal variations associated with the changes in the IMF and solar wind condition, since TADs are known to propagate quasi-horizontally in the thermosphere with velocities close to the local sound speed [e.g., Gardner and Schunk, 2010], or it might as well be that perturbations generated by O^+ precipitation are not large enough to produce any noticeable effect.

One may expect another energy deposition process on the nightside of Mars and Venus. The observed ionospheric convection velocities on Mars and Venus exceed $\sim 1\text{--}5 \text{ km/s}$ above 300 km near the terminator and become chaotic (or form a complicated flow pattern) on the nightside [Knudsen, 1992; Terada *et al.*, 2009;

Table 3. Correlation Coefficients Between the Corrected GW Amplitudes and Upper Thermospheric Temperature (T_0), SZA Where NGIMS Measured $N(\text{Ar}) = 10^5 \text{ cm}^{-3}$, Solar EUV Irradiances Measured in Channel A (17–22 nm), Channel B (0.1–7 nm), and Channel C (121–122 nm), Solar Wind Dynamic Pressure, Solar Wind Density, and Solar Wind Velocity for the Inbound, Outbound, and All Legs^a

	Inbound	Outbound	All
T_0	0.05	0.07	0.05
T_0 (daily averaged)	−0.11	−0.01	−0.07
SZA where $N(\text{Ar}) = 10^5 \text{ cm}^{-3}$	−0.08	−0.14	−0.09
EUV Channel A (17–22 nm)	−0.04	−0.01	−0.03
EUV Channel B (0.1–7 nm)	−0.04	−0.01	−0.03
EUV Channel C (121–122 nm)	−0.07	0.00	−0.04
Solar wind dynamic pressure	−0.06	−0.06	−0.06
Solar wind density	−0.08	−0.08	−0.08
Solar wind velocity	0.04	−0.01	0.02

^aCorrelation coefficient between the daily-averaged corrected GW amplitudes and T_0 is also shown.

Fränz *et al.*, 2010; Chaufray *et al.*, 2014]. Fränz *et al.* [2010] estimated that the transterminator flux of O^+ and O_2^+ ions with a velocity of $\sim 5 \text{ km/s}$ is about 3.1×10^{25} ions/s on Mars, half of which is expected to escape from Mars. The remaining part of the transterminator flux is expected to be lost through recombination in the nightside ionosphere [Knudsen and Miller, 1992]. The kinetic energy of these recombined ions amounts to $\sim 3 \times 10^{25} \text{ eV/s}$, which can be comparable with the energy deposition by the pickup O^+ ions in the midnight and, thus, can be a heat source for generating perturbations

in the nightside thermosphere on Mars (and Venus). The observed higher GW activity on the nightside in Figure 12c is consistent with this scenario. The very weak anticorrelations of the GW amplitudes with the solar wind dynamic pressure and density (Figure 8) might be related to this process, since the transterminator flux is mainly controlled by the terminator ionopause altitude and, thus, by the solar wind dynamic pressure [Cravens *et al.*, 1982].

Our results show that the latitudinal and longitudinal dependences of the corrected amplitudes in the GEO, MSO, and MSE coordinates (Figures 10 and 11) as well as the solar wind parameter dependences (Figure 8) are of the order of a few percent or less, which are less significant compared to the T_0 dependence. These weak dependences make it difficult to clearly identify the sources of the GWs in the Martian upper thermosphere.

5. Conclusions

Global distribution and parameter dependences of GW activity in the Martian upper thermosphere have been analyzed using the Ar density profiles obtained by MAVEN/NGIMS from February 2015 to March 2016. The amplitudes of GWs around the Martian exobase with apparent wavelengths between ~ 100 and $\sim 500 \text{ km}$ show a clear dependence on the background atmospheric temperature (T_0). They also depend on solar zenith angle (SZA) and solar EUV flux, but these dependences occur through the T_0 dependence. The GW amplitudes are inversely proportional to T_0 , suggesting that the wave amplitude growth with height is primarily limited by breaking/saturation due to convective instability. A large part of the GWs distribute around the threshold curves obtained for $\lambda_z = 20\text{--}40 \text{ km}$. Some large amplitude GWs favor longer vertical wavelength modes with $\lambda_z < 100\text{--}200 \text{ km}$. This limitation of GW amplitudes by the convective breaking/saturation is in contrast to Venus and Earth, where other damping processes, like radiative damping, ion drag, and molecular diffusion, are expected to dominate in limiting GW amplitudes in the upper thermosphere [Yigit *et al.*, 2008]. The average amplitude of GWs in the Martian upper thermosphere is $\sim 10\%$ on the dayside and $\sim 20\%$ on the nightside, which is about 2 and 10 times larger than those on Venus and in the low-latitude region of Earth, respectively [Kasprzak *et al.*, 1988; Bruinsma and Forbes, 2008]. Using the corrected GW amplitudes, which are obtained by removing the T_0 dependence from the observed GW amplitudes, we find that the dependences of the average amplitude on latitudes and longitudes in the GEO, MSO, and MSE coordinates as well as on the solar wind parameters are of the order of a few percent or less. Therefore, these dependences are less significant compared to the T_0 dependence. Possible sources of GWs in the Martian upper thermosphere including upward propagation of harmonics from the lower and middle atmosphere and in situ excitation of GWs in the thermosphere by precipitating particles have been discussed, but our statistical analysis could not distinguish between them. Further observations of latitudinal variations of the GW activity at specific seasons as well as a comprehensive theoretical modeling of wave propagation, breaking/saturation, dissipation, and in situ excitation are required.

Acknowledgments

This work was supported by Grant-in-Aid for Scientific Research (B) 15H03731 and for Scientific Research (A) 16H02229 from the Japan Society for the Promotion of Science (JSPS). F.L. is indebted to the program "Système Solaire" of CNES, the French space administration, for its financial support on MAVEN. S.L.E. and E.Y. were supported by NASA through grant NNX13AO36G. The MAVEN project is supported by NASA through the Mars Exploration Program. This work was conducted under NASA's MAVEN Participating Scientist Program (proposal 12-MAVENPS12-0017, PI: K. Seki). The NGIMS, SWIA, MAG, and EUV data are available in the Planetary Data System Archive (http://atmos.nmsu.edu/data_and_services/atmospheres_data/MAVEN/maven_main.html).

References

- Acuña, M. H., et al. (1999), Global distribution of crustal magnetization discovered by the Mars Global Surveyor MAG/ER experiment, *Science*, *284*, 790–793, doi:10.1126/science.284.5415.790.
- Altieri, F., A. Spiga, L. Zasova, G. Bellucci, and J.-P. Bibring (2012), Gravity waves mapped by the OMEGA/MEX instrument through O₂ dayglow at 1.27 μ m: Data analysis and atmospheric modeling, *J. Geophys. Res.*, *117*, E00J08, doi:10.1029/2012JE004065.
- Benna, M., P. R. Mahaffy, J. M. Grebowsky, J. L. Fox, R. V. Yelle, and B. M. Jakosky (2015), First measurements of composition and dynamics of the Martian ionosphere by MAVEN's Neutral Gas and Ion Mass Spectrometer, *Geophys. Res. Lett.*, *42*, 8958–8965, doi:10.1002/2015GL066146.
- Bougher, S. (1995), Comparative thermospheres: Venus and Mars, *Adv. Space Res.*, *15*, 21–45, doi:10.1016/0273-1177(94)00062-6.
- Bougher, S., et al. (2015), Early MAVEN Deep Dip campaign reveals thermosphere and ionosphere variability, *Science*, *350*, doi:10.1126/science.aad0459.
- Bougher, S. W., S. Engel, R. G. Roble, and B. Foster (1999), Comparative terrestrial planet thermospheres: 2. Solar cycle variation of global structure and winds at equinox, *J. Geophys. Res.*, *104*, 16,591–16,611, doi:10.1029/1998JE001019.
- Bougher, S. W., D. Pawlowski, J. M. Bell, S. Nelli, T. McDunn, J. R. Murphy, M. Chizek, and A. Ridley (2015), Mars global ionosphere-thermosphere model: Solar cycle, seasonal, and diurnal variations of the Mars upper atmosphere, *J. Geophys. Res. Planets*, *120*, 311–342, doi:10.1002/2014JE004715.
- Bruinsma, S. L., and J. M. Forbes (2008), Medium- to large-scale density variability as observed by CHAMP, *Space Weather*, *6*, S08002, doi:10.1029/2008SW000411.
- Chaufray, J. Y., R. Modolo, F. Leblanc, G. Chanteur, R. E. Johnson, and J. G. Luhmann (2007), Mars solar wind interaction: Formation of the Martian corona and atmospheric loss to space, *J. Geophys. Res.*, *112*, E09009, doi:10.1029/2007JE002915.
- Chaufray, J.-Y., F. Gonzalez-Galindo, F. Forget, M. Lopez-Valverde, F. Leblanc, R. Modolo, S. Hess, M. Yagi, P.-L. Blelly, and O. Witasse (2014), Three-dimensional Martian ionosphere model: II. Effect of transport processes due to pressure gradients, *J. Geophys. Res. Planets*, *119*, 1614–1636, doi:10.1002/2013JE004551.
- Connerney, J. E. P., M. H. Acuña, P. J. Wasilewski, G. Kletetschka, N. F. Ness, H. Rème, R. P. Lin, and D. L. Mitchell (2001), The global magnetic field of Mars and implications for crustal evolution, *Geophys. Res. Lett.*, *28*, 4015–4018, doi:10.1029/2001GL013619.
- Connerney, J. E. P., J. Espley, P. Lawton, S. Murphy, J. Odom, R. Oliverson, and D. Sheppard (2015), The MAVEN magnetic field investigation, *Space Sci. Rev.*, *195*, 257–291, doi:10.1007/s11214-015-0169-4.
- Cravens, T. E., et al. (1982), Disappearing ionospheres on the nightside of Venus, *Icarus*, *51*, 271–282, doi:10.1016/0019-1035(82)90083-5.
- Creasey, J. E., J. M. Forbes, and D. P. Hinson (2006a), Global and seasonal distribution of gravity wave activity in Mars' lower atmosphere derived from MGS radio occultation data, *Geophys. Res. Lett.*, *33*, L01803, doi:10.1029/2005GL024037.
- Creasey, J. E., J. M. Forbes, and G. M. Keating (2006b), Density variability at scales typical of gravity waves observed in Mars' thermosphere by the MGS accelerometer, *Geophys. Res. Lett.*, *33*, L22814, doi:10.1029/2006GL027583.
- Del Genio, A. D., G. Schubert, and J. M. Straus (1979), Gravity wave propagation in a diffusively separated atmosphere with height-dependent collision frequencies, *J. Geophys. Res.*, *84*, 4371–4378, doi:10.1029/JA084iA08p04371.
- Eckermann, S. D., J. Ma, and X. Zhu (2011), Scale-dependent infrared radiative damping rates on Mars and their role in the deposition of gravity-wave momentum flux, *Icarus*, *211*, 429–442, doi:10.1016/j.icarus.2010.10.029.
- England, S. L., G. Liu, E. Yiğit, P. R. Mahaffy, M. Elrod, M. Benna, H. Nakagawa, N. Terada, and B. Jakosky (2016), MAVEN NGIMS observations of atmospheric gravity waves in the Martian thermosphere, *J. Geophys. Res. Space Physics*, *121*, doi:10.1002/2016JA023475.
- Eparvier, F. G., P. C. Chamberlin, T. N. Woods, and E. M. B. Thiemann (2015), The solar extreme ultraviolet monitor for MAVEN, *Space Sci. Rev.*, *195*, 293–301, doi:10.1007/s11214-015-0195-2.
- Fang, X., S. W. Bougher, R. E. Johnson, J. G. Luhmann, Y. Ma, Y.-C. Wang, and M. W. Liemohn (2013), The importance of pickup oxygen ion precipitation to the Mars upper atmosphere under extreme solar wind conditions, *Geophys. Res. Lett.*, *40*, 1922–1927, doi:10.1002/grl.50415.
- Forbes, J. M., S. Bruinsma, and F. G. Lemoine (2006), Solar rotation effects on the thermospheres of Mars and Earth, *Science*, *312*, 1366–1368, doi:10.1126/science.1126389.
- Fox, J. L., and A. Dalgarno (1979), Ionization, luminosity, and heating of the upper atmosphere of Mars, *J. Geophys. Res.*, *84*, 7315–7333, doi:10.1029/JA084iA12p07315.
- Fränz, M., E. Dubinin, E. Nielsen, J. Woch, S. Barabash, R. Lundin, and A. Fedorov (2010), Transterminator ion flow in the Martian ionosphere, *Planet. Space Sci.*, *58*, 1442–1454, doi:10.1016/j.pss.2010.06.009.
- Fritts, D. C. (1984), Gravity wave saturation in the middle atmosphere: A review of theory and observations, *Rev. Geophys.*, *22*, 275–308, doi:10.1029/RG022i003p00275.
- Fritts, D. C., and M. J. Alexander (2003), Gravity wave dynamics and effects in the middle atmosphere, *Rev. Geophys.*, *41*(1), 1003, doi:10.1029/2001RG000106.
- Fritts, D. C., and P. K. Rastogi (1985), Convective and dynamical instabilities due to gravity wave motions in the lower and middle atmosphere: Theory and observations, *Radio Sci.*, *20*, 1247–1277, doi:10.1029/RS020i006p01247.
- Fritts, D. C., L. Wang, and R. H. Tolson (2006), Mean and gravity wave structures and variability in the Mars upper atmosphere inferred from Mars Global Surveyor and Mars Odyssey aerobraking densities, *J. Geophys. Res.*, *111*, A12304, doi:10.1029/2006JA011897.
- Fujiwara, H., and Y. Miyoshi (2006), Characteristics of the large-scale traveling atmospheric disturbances during geomagnetically quiet and disturbed periods simulated by a whole atmosphere general circulation model, *Geophys. Res. Lett.*, *33*, L20108, doi:10.1029/2006GL027103.
- Fujiwara, H., and Y. Miyoshi (2009), Global distribution of the thermospheric disturbances produced by effects from the upper and lower regions: Simulations by a whole atmosphere GCM, *Earth Planets Space*, *61*, 463–470, doi:10.1186/BF03353163.
- Gardner, L. C., and R. W. Schunk (2010), Generation of traveling atmospheric disturbances during pulsating geomagnetic storms, *J. Geophys. Res.*, *115*, A08314, doi:10.1029/2009JA015129.
- González-Galindo, F., F. Forget, M. A. López-Valverde, M. Angelats i Coll, and E. Millour (2009), A ground-to-exosphere Martian general circulation model: 1. Seasonal, diurnal, and solar cycle variation of thermospheric temperatures, *J. Geophys. Res.*, *114*, E04001, doi:10.1029/2008JE003246.
- Hines, C. O. (1960), Internal atmospheric gravity waves at ionospheric heights, *Can. J. Phys.*, *38*, 1441–1481, doi:10.1139/p60-150.
- Hocke, K., and K. Schlegel (1996), A review of atmospheric gravity waves and travelling ionospheric disturbances: 1982–1995, *Ann. Geophys.*, *14*, 917–940, doi:10.1007/s00585-996-0917-6.
- Imamura, T., A. Watanabe, and Y. Maejima (2016), Convective generation and vertical propagation of fast gravity waves on Mars: One- and two-dimensional modeling, *Icarus*, *267*, 51–63, doi:10.1016/j.icarus.2015.12.005.

- Jakosky, B. M., et al. (2015), The Mars atmosphere and volatile evolution (MAVEN) mission, *Space Sci. Rev.*, *195*, 3–48, doi:10.1007/s11214-015-0139-x.
- Kasprzak, W. T., A. E. Hedin, H. G. Mayr, and H. B. Niemann (1988), Wavelike perturbations observed in the neutral thermosphere of Venus, *J. Geophys. Res.*, *93*, 11,237–11,245, doi:10.1029/JA093iA10p11237.
- Keating, G. M., and S. W. Bougher (1992), Isolation of major Venus thermospheric cooling mechanism and implications for Earth and Mars, *J. Geophys. Res.*, *97*, 4189–4197, doi:10.1029/91JA02444.
- Knipp, D. J., W. K. Tobiska, and B. A. Emery (2004), Direct and indirect thermospheric heating sources for solar cycles 21–23, *Sol. Phys.*, *224*, 495–505, doi:10.1007/s11207-005-6393-4.
- Knudsen, W. C. (1992), The Venus ionosphere from in situ measurements, in *Venus and Mars: Atmospheres, Ionospheres, and Solar Wind Interactions*, edited by J. G. Luhmann, M. Tatallyay, and R. O. Pepin, AGU, Washington, D. C., doi:10.1029/GM066p0237.
- Knudsen, W. C., and K. L. Miller (1992), The Venus transterminator ion flux at solar maximum, *J. Geophys. Res.*, *97*, 17,165–17,167, doi:10.1029/92JA01460.
- Kuroda, T., A. S. Medvedev, E. Yiğit, and P. Hartogh (2015), A global view of gravity waves in the Martian atmosphere inferred from a high-resolution general circulation model, *Geophys. Res. Lett.*, *42*, 9213–9222, doi:10.1002/2015GL066332.
- Kuroda, T., A. S. Medvedev, E. Yiğit, and P. Hartogh (2016), Global distribution of gravity wave sources and fields in the Martian atmosphere during equinox and solstice inferred from a high-resolution general circulation model, *J. Atmos. Sci.*, *73*, 4895–4909, doi:10.1175/JAS-D-16-0142.1.
- Leblanc, F., and R. E. Johnson (2002), Role of molecular species in pickup ion sputtering of the Martian atmosphere, *J. Geophys. Res.*, *107*(E2), 5010, doi:10.1029/2000JE001473.
- Lindzen, R. S. (1973), Wave-mean flow interactions in the upper atmosphere, *Boundary Layer Meteorol.*, *4*, 327–343, doi:10.1007/BF02265242.
- Luhmann, J. G., and J. U. Kozyra (1991), Dayside pickup oxygen ion precipitation at Venus and Mars: Spatial distributions, energy deposition and consequences, *J. Geophys. Res.*, *96*, 5457–5467, doi:10.1029/90JA01753.
- Mahaffy, P. R., et al. (2014), The neutral gas and ion mass spectrometer on the Mars atmosphere and volatile evolution mission, *Space Sci. Rev.*, *195*, 49–73, doi:10.1007/s11214-014-0091-1.
- Mahaffy, P. R., M. Benna, M. Elrod, R. V. Yelle, S. W. Bougher, S. W. Stone, and B. M. Jakosky (2015), Structure and composition of the neutral upper atmosphere of Mars from the MAVEN NGIMS investigation, *Geophys. Res. Lett.*, *42*, 8951–8957, doi:10.1002/2015GL065329.
- Mayr, H. G., I. Harris, F. A. Herrero, N. W. Spencer, F. Varosi, and W. D. Pesnell (1990), Thermospheric gravity waves: Observations and interpretation using the transfer function model (TEM), *Space Sci. Rev.*, *54*, 297–375, doi:10.1007/BF00177800.
- Medvedev, A. S., and E. Yiğit (2012), Thermal effects of internal gravity waves in the Martian upper atmosphere, *Geophys. Res. Lett.*, *39*, L05201, doi:10.1029/2012GL050852.
- Medvedev, A. S., E. Yiğit, and P. Hartogh (2011a), Estimates of gravity wave drag on Mars: Indication of a possible lower thermospheric wind reversal, *Icarus*, *211*, 909–912, doi:10.1016/j.icarus.2010.10.013.
- Medvedev, A. S., E. Yiğit, P. Hartogh, and E. Becker (2011b), Influence of gravity waves on the Martian atmosphere: General circulation modeling, *J. Geophys. Res.*, *116*, E10004, doi:10.1029/2011JE003848.
- Medvedev, A. S., E. Yiğit, T. Kuroda, and P. Hartogh (2013), General circulation modeling of the Martian upper atmosphere during global dust storms, *J. Geophys. Res. Planets*, *118*, 2234–2246, doi:10.1002/jgre.20163.
- Medvedev, A. S., F. González-Galindo, E. Yiğit, A. G. Feofilov, F. Forget, and P. Hartogh (2015), Cooling of the Martian thermosphere by CO₂ radiation and gravity waves: An intercomparison study with two general circulation models, *J. Geophys. Res. Planets*, *120*, 913–927, doi:10.1002/2015JE004802.
- Medvedev, A. S., et al. (2016), Comparison of the Martian thermospheric density and temperature from IUVS/MAVEN data and general circulation modeling, *Geophys. Res. Lett.*, *43*, 3095–3104, doi:10.1002/2016GL068388.
- Miyoshi, Y., and H. Fujiwara (2009), Gravity waves in the equatorial thermosphere and their relation to lower atmospheric variability, *Earth Planets Space*, *61*, 471–478, doi:10.1186/BF03353164.
- Miyoshi, Y., J. M. Forbes, and Y. Moulden (2011), A new perspective on gravity waves in the Martian atmosphere: Sources and features, *J. Geophys. Res.*, *116*, E09009, doi:10.1029/2011JE003800.
- Miyoshi, Y., H. Fujiwara, H. Jin, and H. Shinagawa (2014), A global view of gravity waves in the thermosphere simulated by a general circulation model, *J. Geophys. Res. Space Physics*, *119*, 5807–5820, doi:10.1002/2014JA019848.
- Oliver, W. L., Y. Otsuka, M. Sato, T. Takami, and S. Fukao (1997), A climatology of F region gravity wave propagation over the middle and upper atmosphere radar, *J. Geophys. Res.*, *102*, 14,499–14,512, doi:10.1029/97JA00491.
- Parish, H. F., G. Schubert, M. P. Hickey, and R. L. Walterscheid (2009), Propagation of tropospheric gravity waves into the upper atmosphere of Mars, *Icarus*, *203*, 28–37, doi:10.1016/j.icarus.2009.04.031.
- Prölss, G. W. (1993), Common origin of positive ionospheric storms at middle latitudes and the geomagnetic activity effect at low latitudes, *J. Geophys. Res.*, *98*, 5981–5991, doi:10.1029/92JA02777.
- Sato, K., S. Watanabe, Y. Kawatani, Y. Tomikawa, K. Miyazaki, and M. Takahashi (2009), On the origins of mesospheric gravity waves, *Geophys. Res. Lett.*, *36*, L19801, doi:10.1029/2009GL039908.
- Smith, S. A., D. C. Fritts, and T. E. VanZandt (1987), Evidence for a saturated spectrum of atmospheric gravity waves, *J. Atmos. Sci.*, *44*, 1404–1410, doi:10.1175/1520-0469(1987)044<1404:EFASSO>2.0.CO;2.
- Sonmor, L. G., and G. P. Klaassen (1997), Toward a unified theory of gravity wave stability, *J. Atmos. Sci.*, *54*, 2655–2680, doi:10.1175/1520-0469(1997)054<2655:TAUTOG>2.0.CO;2.
- Spiga, A., F. González-Galindo, M.-Á. López-Valverde, and F. Forget (2012), Gravity waves, cold pockets and CO₂ clouds in the Martian mesosphere, *Geophys. Res. Lett.*, *39*, L02201, doi:10.1029/2011GL050343.
- Terada, K., N. Terada, H. Shinagawa, H. Fujiwara, Y. Kasaba, K. Seki, F. Leblanc, J.-Y. Chaufray, and R. Modolo (2016), A full-particle Martian upper thermosphere-exosphere model using the DSMC method, *J. Geophys. Res. Planets*, *121*, 1429–1444, doi:10.1002/2015JE004961.
- Terada, N., H. Shinagawa, T. Tanaka, K. Murawski, and K. Terada (2009), A three-dimensional, multispecies, comprehensive MHD model of the solar wind interaction with the planet Venus, *J. Geophys. Res.*, *114*, A09208, doi:10.1029/2008JA013937.
- Tsugawa, T., A. Saito, and Y. Otsuka (2004), A statistical study of large-scale traveling ionospheric disturbances using the GPS network in Japan, *J. Geophys. Res.*, *109*, A06302, doi:10.1029/2003JA010302.
- Vadas, S. L. (2007), Horizontal and vertical propagation and dissipation of gravity waves in the thermosphere from lower atmospheric and thermospheric sources, *J. Geophys. Res.*, *112*, A06305, doi:10.1029/2006JA011845.
- Vadas, S. L., and H. Liu (2009), Generation of large-scale gravity waves and neutral winds in the thermosphere from the dissipation of convectively generated gravity waves, *J. Geophys. Res.*, *114*, A10310, doi:10.1029/2009JA014108.

- Walterscheid, R. L., M. P. Hickey, and G. Schubert (2013), Wave heating and Jeans escape in the Martian upper atmosphere, *J. Geophys. Res. Planets*, *118*, 2413–2422, doi:10.1002/jgre.20164.
- Yiğit, E., and A. S. Medvedev (2009), Heating and cooling of the thermosphere by internal gravity waves, *Geophys. Res. Lett.*, *36*, L14807, doi:10.1029/2009GL038507.
- Yiğit, E., and A. S. Medvedev (2010), Gravity waves in the thermosphere during low and high solar activity: Simulation study, *J. Geophys. Res.*, *115*, A00G02, doi:10.1029/2009JA015106.
- Yiğit, E., and A. S. Medvedev (2015), Internal wave coupling processes in Earth's atmosphere, *Adv. Space Res.*, *55*, 983–1003, doi:10.1016/j.asr.2014.11.020.
- Yiğit, E., A. D. Aylward, and A. S. Medvedev (2008), Parameterization of the effects of vertically propagating gravity waves for thermosphere general circulation models: Sensitivity study, *J. Geophys. Res.*, *113*, D19106, doi:10.1029/2008JD010135.
- Yiğit, E., A. S. Medvedev, A. D. Aylward, P. Hartogh, and M. J. Harris (2009), Modeling the effects of gravity wave momentum deposition on the general circulation above the turbopause, *J. Geophys. Res.*, *114*, D07101, doi:10.1029/2008JD011132.
- Yiğit, E., A. S. Medvedev, and P. Hartogh (2015a), Gravity waves and high-altitude CO₂ ice cloud formation in the Martian atmosphere, *Geophys. Res. Lett.*, *42*, 4294–4300, doi:10.1002/2015GL064275.
- Yiğit, E., S. L. England, G. Liu, A. S. Medvedev, P. R. Mahaffy, T. Kuroda, and B. M. Jakosky (2015b), High-altitude gravity waves in the Martian thermosphere observed by MAVEN/NGIMS and modeled by a gravity wave scheme, *Geophys. Res. Lett.*, *42*, 8993–9000, doi:10.1002/2015GL065307.
- Yiğit, E., P. K. Knížová, K. Georgieva, and W. Ward (2016), A review of vertical coupling in the Atmosphere–Ionosphere system: Effects of waves, sudden stratospheric warmings, space weather, and of solar activity, *J. Atmos. Sol. Terr. Phys.*, *141*, 1–12, doi:10.1016/j.jastp.2016.02.011.